Active–Passive Remote Sensing Identification of Underground Coal Fire Zones With Joint Constraints of Temperature and Surface Deformation Time Series

Yu Chen, Zhihui Suo, Jie Li, Jun Wei, Fei Cao, Huahai Sun, Huaizhan Li, Yandong Gao, Qian Li, Yinglong Yue, and Kaimin Xu

***Abstract*—Coal fire is a geological disaster that causes resource waste and environmental pollution globally. Accurate identification of the spatial location of coal fires is critical for effective coal fire governance. However, existing methods for identifying coal fire zones have problems, such as a high omission and misclassification ratio and insufficient consideration of the temporal variation in temperature. Therefore, this article proposed a temporal temperature anomaly extraction algorithm based on adaptive windows (TTAE-AW) to extract temporal temperature anomaly information. Moreover, the spatial coverage of deformation monitoring points was improved using distributed scatterer interferometric synthetic aperture radar (DS-InSAR), and then a double-threshold two-stage filter method (DTTF) was proposed to accurately identify the spatial location of coal fire zones. The Rujigou mining area in Ningxia (China) was chosen as the region of study. Results showed that the temperature anomalies extracted using the TTAE-AW method are more concentrated in coal fire zones and that the amount in different seasons is more stable. The average accuracy and Kappa coefficient were improved by 15.5% and 0.345, respectively, over those of the conventional method. Compared with the small baselines subset InSAR approach, the DS-InSAR technique has 158% higher spatial coverage for monitoring coal fire zones. Compared with in situ observations of coal fire points, the accuracy and Kappa coefficient of the spatial location of fire zones obtained using the DTTF method were 91% and 0.77, respectively, demonstrating that the proposed method can provide reliable technical support for coal fire monitoring and management.**

***Index Terms*—Collaborative analysis, distributed scatterer interferometric synthetic aperture radar (DS-InSAR), surface deformation, thermal infrared (TIR) remote sensing, time-series temperature anomaly extraction (TAE), underground coal fire identification.**

Manuscript received 13 August 2023; revised 17 October 2023; accepted 14 November 2023. Date of publication 28 November 2023; date of current version 6 December 2023. This work was supported in part by the National Natural Science Foundation of China under Grant 42171312, Grant 42001409, and Grant 42174048, in part by the Basic Research Program of Xuzhou under Grant KC23049, in part by the Open Fund of Key Laboratory of Geographic Information Science (Ministry of Education), East China Normal University under Grant KLGIS2023A02, and in part by the Natural Science Foundation of Jiangsu Province under Grant BK20220158. *(Yu Chen and Zhihui Suo are co-first authors.) (Corresponding author: Yu Chen.)*

Yu Chen is with the School of Environment Science and Spatial Informatics, China University of Mining and Technology, Xuzhou 221116, China, and also with the Key Laboratory of Geographic Information Science (Ministry of Education), East China Normal University, Shanghai 200241, China (e-mail: chenyu@cumt.edu.cn).

Zhihui Suo, Jie Li, Huaizhan Li, Yandong Gao, and Qian Li are with the School of Environment Science and Spatial Informatics, China University of Mining and Technology, Xuzhou 221116, China (e-mail: suozh@cumt.edu.cn; yunhuili@cumt.edu.cn; lihuaizhan@cumt.edu.cn; ydgao@cumt.edu.cn; li_qian@cumt.edu.cn).

Jun Wei, Fei Cao, and Huahai Sun are with the Xinjiang Uygur Autonomous Region Mine Safety Service and Guarantee Center, Urumqi 830017, China (e-mail: weijunwxx@163.com; figo6507804@163.com; 297228108@qq.com).

Yinglong Yue is with the Ningxia Coal Industry Company Limited, Yinchuan 750000, China (e-mail: yueying52013140@126.com).

Kaimin Xu is with the Shaanxi Star Times Technology Development Company Limited, Xi'an 710000, China (e-mail: 380974681@qq.com).

Digital Object Identifier 10.1109/JSTARS.2023.3335293

I. Introduction

UNDERGROUND coal fires are characterized as large-scale coalfield fires that develop over time due to either human factors or spontaneous ignition of a coal seam [1], [2], [3]. Currently, there are approximately 10 000 underground coal fire zones globally. The situation is most critical in China, USA, India, and Australia, but also in other countries and regions with abundant coal reserves. The long-term burning of underground coal fires causes serious resource loss, atmospheric pollution, and increases global warming. In addition, it can result in ground settlement, surface cracks, and geological disasters [4], [5], [6]. Therefore, it is important to accurately identify and dynamically monitor coal fire zones to support the extinguishing and warning of coal fire disasters.

Currently, the five main approaches for monitoring and detecting underground coal fires comprise physical, chemical, thermal, drilling, and remote sensing methods [7], [8], [9], [10], [11], [12]. Although the first four are commonly used and considered effective, the required field research is time consuming and expensive. Moreover, it is difficult to monitor zones with large fires. Remote sensing has the advantages of large-area synchronous observation, traceability, and economy, and it has gradually become one of the mainstream methods for coal fire detection in recent years [13], [14], [15], [16]. Heat from combustion is transferred to the surface resulting in higher surface temperatures in coal fire zones than in noncoal fire zones [17], [18]. Consequently, thermal infrared (TIR) imagery can be used to invert surface temperatures, extract temperature anomaly zones, and identify the spatial extent of fire zones. Although this is the main approach when using remote sensing technology to detect coal fire zones, choosing a suitable temperature threshold is a difficult but fundamental part of the process [19], [20], [21], [22]. Methods commonly used for temperature anomaly extraction (TAE) can be divided into two

main categories: single-threshold algorithms and multithreshold algorithms. Single-threshold algorithms mainly include the fixed threshold algorithm (FTA) [23], gradient threshold algorithm [24], adaptive gradient threshold algorithm [25], and spatiotemporal temperature-based thresholding algorithm [26]. The main multithreshold algorithm is the TAE algorithm [27]. Single-threshold algorithms select a fixed threshold for the entire image to extract temperature anomalies. This method is convenient and widely applied, but it can be subjective and lead to omission and misclassification of temperature anomalies. The TAE method utilizes local threshold selection to extract temperature anomaly zones, leading to reduction in false detection rates and enhancement in detection accuracy. This approach effectively addresses the limitations of single-threshold algorithms, but it does lack stability. For example, the TAE results are greatly affected by window size, and the single criterion used for selecting temperature anomaly pixels within the window affects recognition accuracy. In addition, the existing algorithms use independent images to identify temperature anomalies and do not consider the fact that coal combustion is a continuous process temporally. Thus, the accuracy of temperature anomaly identification in fire zones is reduced. To address the above problems, this article developed a temporal TAE algorithm based on adaptive windows (TTAE-AW). The algorithm was designed with an AW and multiple filtering criteria within the window. Moreover, the method also considers the temporal continuity of coal fire combustion. Ultimately, the time parameter is used to obtain temporal temperature anomaly information via time-series analysis.

Because of the influence of solar radiation and the poor spatial resolution of TIR remote sensing images, temperature anomaly information is often insufficient for accurate identification of fire zones [28]. Therefore, some studies considered surface deformation information to identify coal fire zones using the feature that underground coal fires trigger surface deformation [12], [23], [24], [26], [29], [30]. However, surface deformation in coal fire zones is complex and often accompanied by different degrees of decoherence. Traditional time-series interferometric synthetic aperture radar (InSAR) techniques sometimes fail to obtain comprehensive deformation information [12], [24], [26]. Therefore, this article adopted the distributed scatterer (DS)-InSAR technique to improve the coherent point density by means of homogeneous point identification and phase optimization. Then, the line-of-sight (LOS) surface deformation rate was solved and the surface deformation anomaly information extracted.

Currently, the main techniques used for identification of coal fire zones that combine temperature and deformation anomaly information are the overlay analysis (OA) [23], [31] and the two-stage bandpass filter methods [24], [26]. The OA method is dependent on the intersection of temperature and deformation anomalies to obtain the coal fire zones. The algorithm is simple but its accuracy is low. In the two-stage bandpass filter method, the temperature and deformation anomaly information intersect on the window and the loss ratio of the temperature anomaly data is solved. Then, the loss ratio threshold is used to filter the temperature anomaly pixels and the retained temperature anomaly pixels represent the identified fire zones. However, this method utilizes a single artificially formulated loss ratio threshold, which leads to unstable results in fire zone identification. Therefore, this article proposed using a double-threshold two-stage filter (DTTF) method, which includes OA and double loss ratio threshold filtering to identify fire zones. Meanwhile, to reduce human intervention, statistical methods were used to determine the double loss ratio thresholds.

This article focused on the Rujigou mine in the Ningxia Hui Autonomous Region of China, which is a typical mining area with a history of coal fire burning that extends over 300 years. Overall, 29 Landsat-8 satellite optical remote sensing images and 35 C-band Sentinel-1A SAR images were combined to verify the applicability of the method.

The rest of this article is organized as follows. Section II provides details of the active–passive remote sensing identification method for underground coal fire zones with joint constraints of temperature anomaly and surface deformation time series, including the temperature inversion method, the TTAE-AW, the surface deformation anomaly extraction method, and the DTTF fire zone identification method. Section III describes the study area and the datasets used. Section IV provides analysis of the study results. Section V discusses the selection of temporal temperature thresholds and the filtering of suspected fire zones. Finally, Section VI concludes this article.

II. Methodology

This article proposed an active–passive remote sensing method for identification of underground coal fire zones. It includes the joint constraints of temperature anomaly and surface deformation time series to resolve the problems of single-threshold selection, solidification of window size, strong subjectivity of parameter setting, and failure to consider the temporal continuity of coal fire combustion in current methods used for TAE and fire zone identification. First, the single-window algorithm was employed to invert the ground temperature. Then, the temporal temperature anomaly information was extracted using the TTAE-AW method. The DS-InSAR technique was utilized to acquire the LOS surface deformation rate and to extract surface deformation anomaly information. Finally, the DTTF method was applied to combine the information of time-series temperature anomalies and surface deformation anomalies to identify the location of underground coal fires in the Rujigou mine. The workflow of the proposed method is illustrated in Fig. 1.

A. Surface Temperature Inversion

Radiometric calibration and atmospheric correction were applied to multitemporal Landsat-8 images, and then the single-window algorithm of Qin et al. [32] was used for surface temperature inversion (Fig. 1).

The core formulas are expressed as follows:

$$T_S = [a \times (1 - C - D) + (b \times (1 - C - D) + C + D) \times T_6 - D \times T_a]/C \quad (1)$$

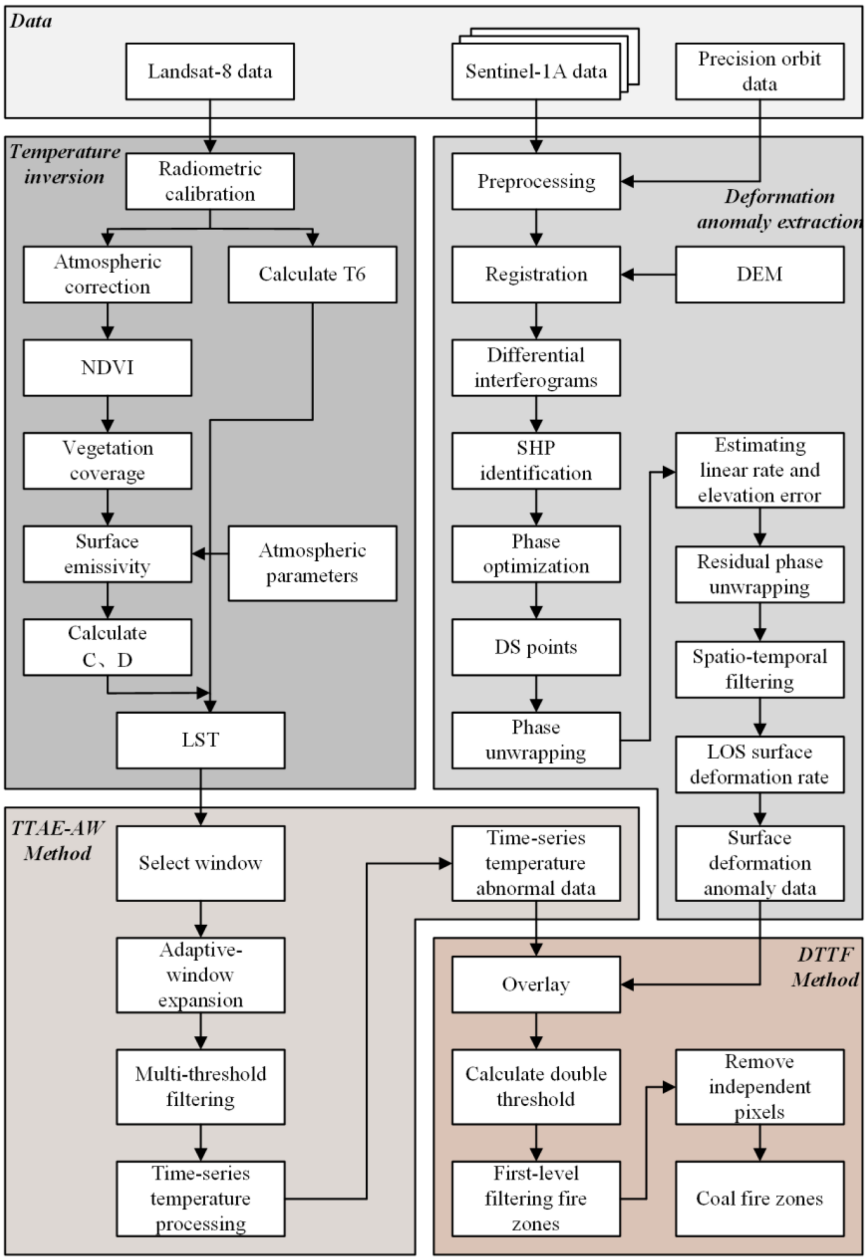

Fig. 1. Workflow of the proposed method.

$$T_6 = K_2 / \ln(K_1 / B(T_S) + 1) \tag{2}$$

$$C = \varepsilon \times \tau \tag{3}$$

$$D = (1 - t) \times (1 + (1 - \varepsilon) \times \tau) \tag{4}$$

where T_S is the surface temperature; a and b are constants with values of -67.355351 and 0.458606, respectively; T_a is the average atmospheric action temperature, which is obtained from a linear relationship with the near-surface temperature during satellite transit; T_6 is the brightness temperature of Landsat-8 band 10; and C and D are intermediate variables, calculated using (3) and (4). In (2), K_1 and K_2 are constants preset before the launch of Landsat-8 satellite with values of 607.76 and 1260.56, respectively, and $B(T_S)$ is the radiation intensity received by the satellite sensor. In (3) and (4), ε is the land surface emissivity, which is obtained by calculating the normalized difference vegetation index with vegetation coverage; and τ is the atmospheric transmittance obtained by calculating the atmospheric profile parameters from the website provided by NASA (https://atmcorr.gsfc.nasa.gov/).

B. Temporal Temperature Anomaly Extraction Algorithm Based on Adaptive Windows (TTAE-AW)

This article proposed the TTAE-AW method to overcome the problems of current TAE algorithms, such as the single threshold value, influence of window size, and failure to consider the combustion continuity of coal fires (Fig. 2). The method consists

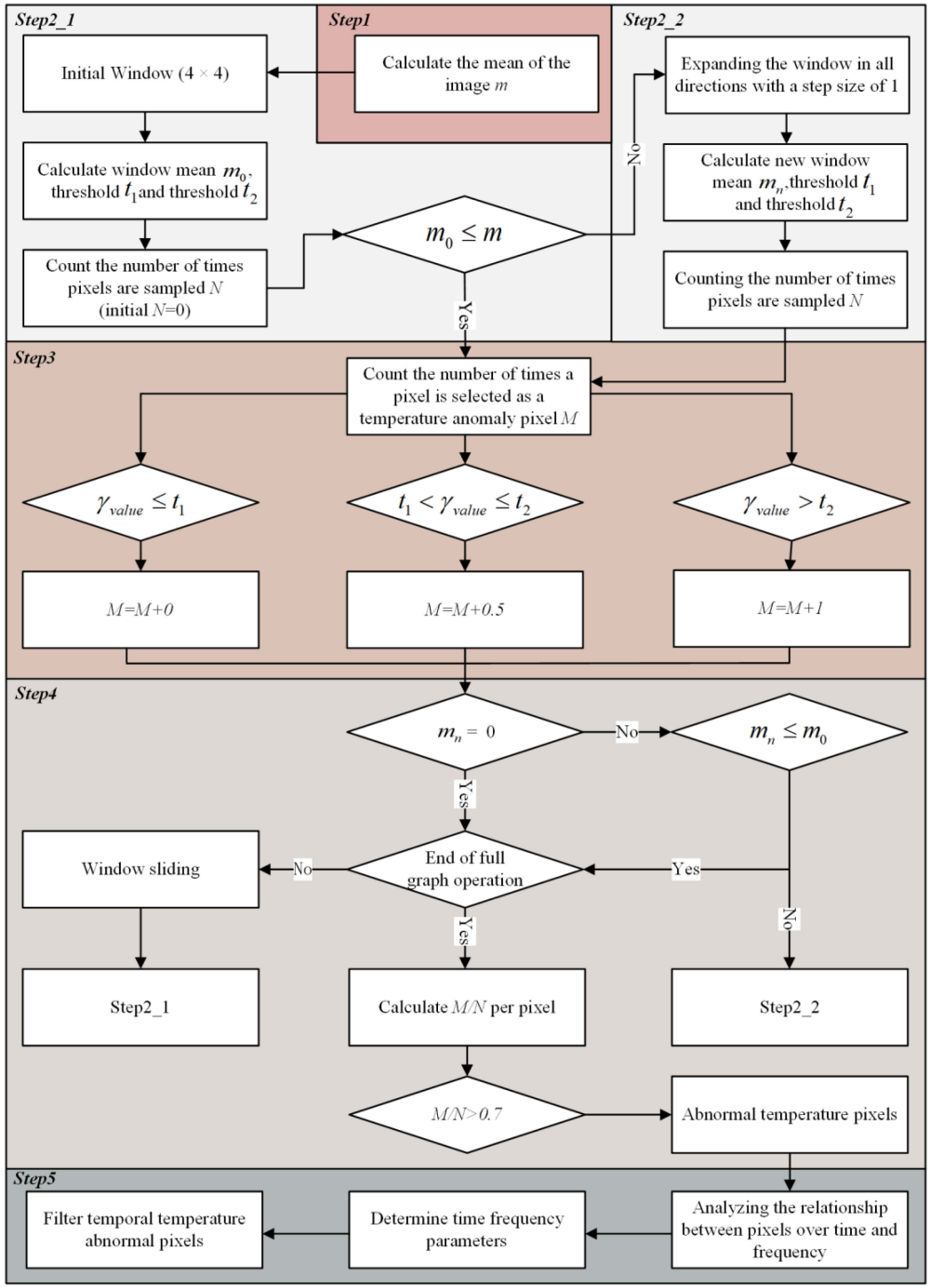

Fig. 2. Schematic of the TTAE-AW algorithm flow.

of TAE algorithm based on the AW (TAE-AW) and a time-series processing method.

1) TAE-AW Algorithm:

1) *Step1:* The mean value m of the entire image surface temperature is calculated.
2) *Step2:* Running Step2_1 (Fig. 2). The starting window size is chosen as 4×4. Then, the mean value m_0, the threshold t_1 (standard deviation plus mean value), and t_2 (double standard deviation plus mean value) of the pixels within the window are calculated. The number of times (N) that pixels are sampled within the window is calculated (whenever a pixel is sampled, the original value of N is increased by 1). Then, the relationship between the window mean m_0 and the entire image mean m is determined. If $m_0 \leq m$, the window is no longer expanded and Step3 is run directly (Fig. 2). If $m_0 > m$, Step2_2 is run (Fig. 2), and the window is spread around in steps of 1. The mean value m_n, the threshold t_1 and t_2, and the number of samples N of the pixels in the new window are calculated. Then, Step3 is run (Fig. 2).

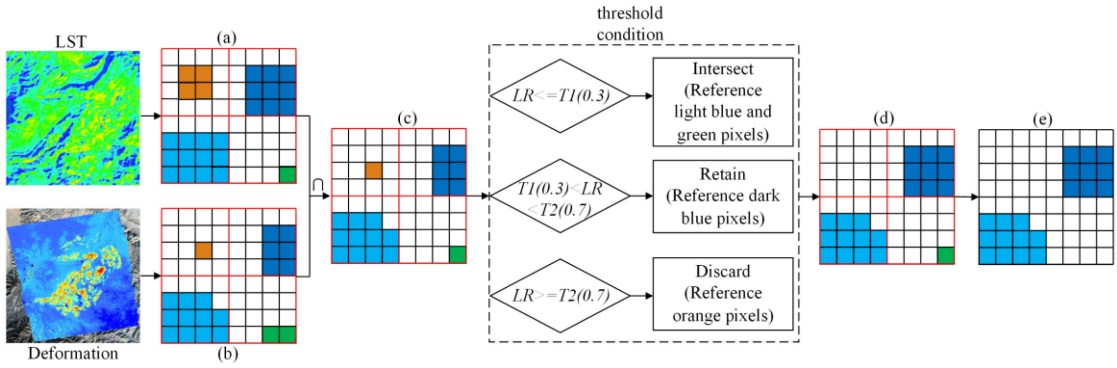

Fig. 3. Flow chart of the DTTF algorithm. Temperature anomaly image (a) and deformation anomaly image (b) are extracted based on the land surface temperature image and deformation image, respectively. The window size is set to 4×4 as in the four parts divided by the red line segment in image (a). The corresponding pixels of images (a) and (b) are intersected to obtain image (c). Assuming that the solved double thresholds $T1$ and $T2$ are 0.3 and 0.7, respectively, then image (d) is obtained for the four window pixels of image (c) according to the threshold condition. Finally, the independent pixels are removed to obtain the final fire zone identification image (e).

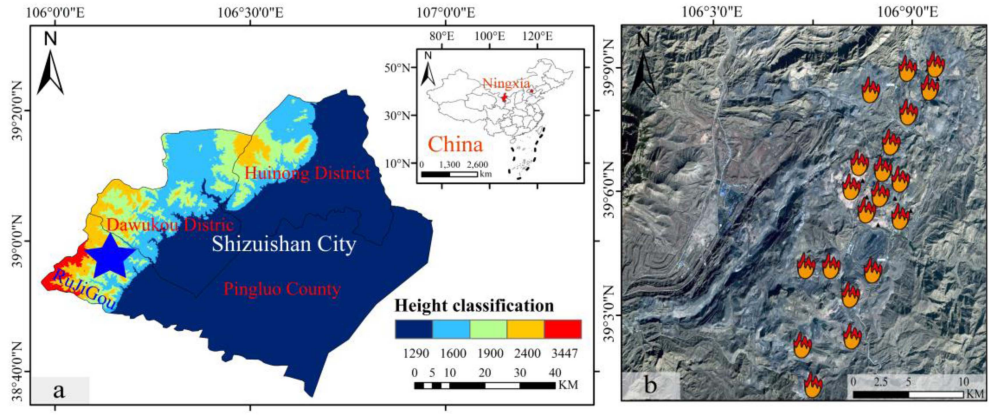

Fig. 4. Geographical overview of Rujigou. (a) Study area location and the DEM. The blue triangle in the figure marks the Rujigou mine. (b) Schematic of coal fire zones in the Rujigou area.

3) *Step3:* Running Step3. The number of times a pixel is selected as a temperature anomaly pixel is calculated (M). If the pixel value $\gamma_{\text{value}} \leq t_1$, it is considered that the pixel is not a temperature anomaly pixel and the value of M remains unchanged. If $t_1 < \gamma_{\text{value}} \leq t_2$, the pixel is considered a low-frequency temperature anomaly pixel and the original value of M is increased by 0.5. If $\gamma_{\text{value}} > t_2$, the pixel is considered a high-frequency temperature anomaly pixel and the original value of M is increased by 1.
4) *Step4:* The value of m_n is determined (Fig. 2, Step4). If $m_n = 0$, it means that the window is not expanded. At this time, it is necessary to determine whether the entire image has finished processing; if not, the window is slid and Step2_1 is run again. If $m_n! = 0$, the window is expanded. If $m_n > m_0$, then Step2_2 is run. If $m_n \leq m_0$, it is necessary to determine whether the entire image has finished running; if not, the window is slid and Step2_1 is run again. After running the entire image, M/N is calculated on a pixel-by-pixel basis. When $M/N > 0.7$, the pixel is selected as a temperature anomaly pixel. A temperature anomaly image is composed of temperature anomaly pixels.

This method extracts temperature anomaly information without determining the size of the sliding window. The window will change adaptively according to the mean of the pixel compared with the threshold value. At the same time, multiple thresholds are used to filter temperature anomaly pixels to avoid omission and misclassification of temperature anomaly zones.

2) Temperature Anomaly of Time-Series Extraction Method: Currently, the information of combined temperature anomalies and surface deformation used to identify fire zones often suffers from large numbers of omissions and misclassifications of coal fire zones [24], [26]. This is because the temperature anomaly information is obtained only for a certain moment, whereas coal fire burning is a continuous process temporally. Therefore, the extracted temperature anomaly information is processed as a time series. First, a time parameter is introduced to count the time frequency of the corresponding pixels for all temperature anomaly images. Then, the time frequency is analyzed and the time frequency threshold (T_f) is determined. Pixels with time

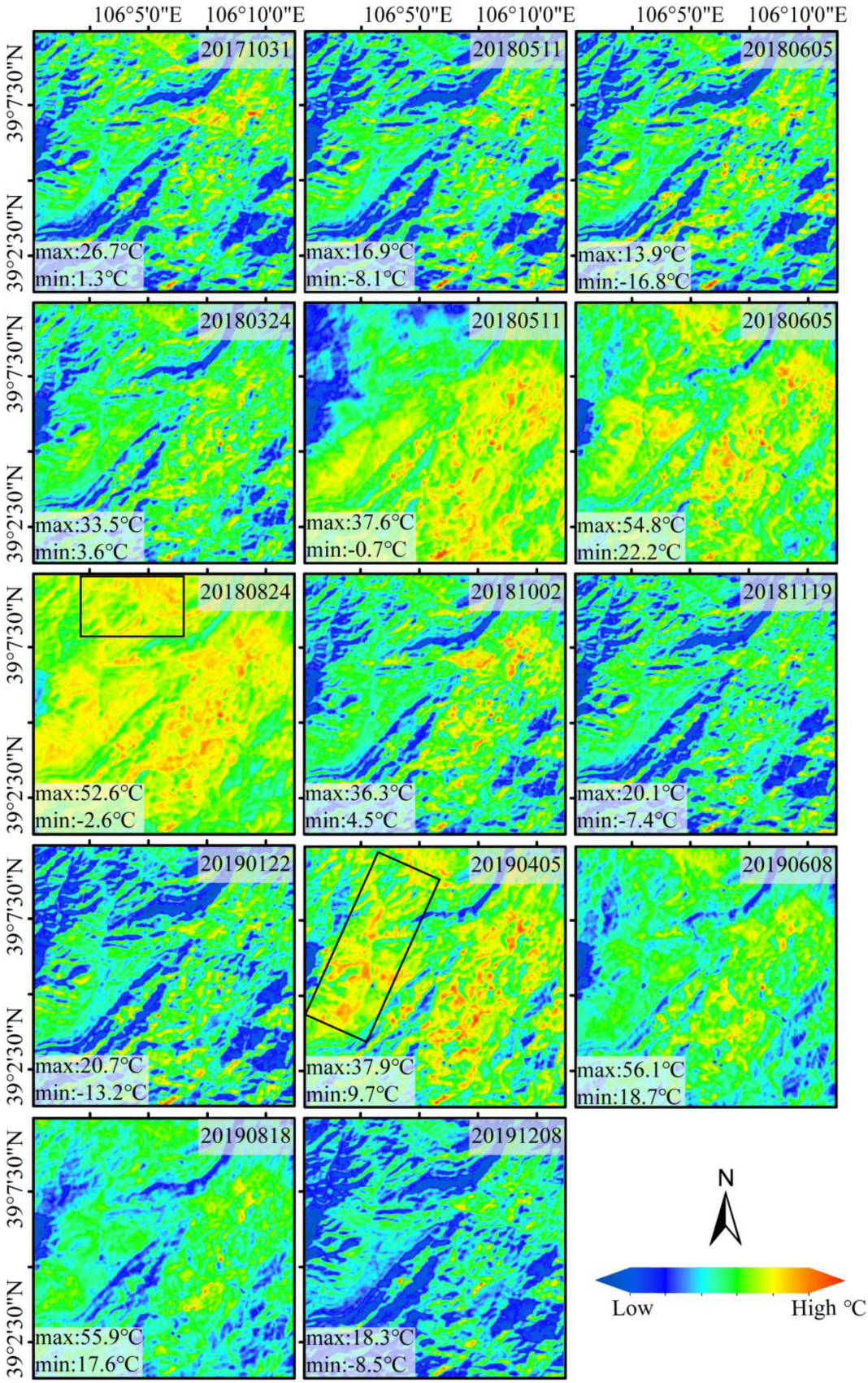

(a)

Fig. 5. (a) Results of surface temperature inversion using single-window algorithm for certain periods in the study area.

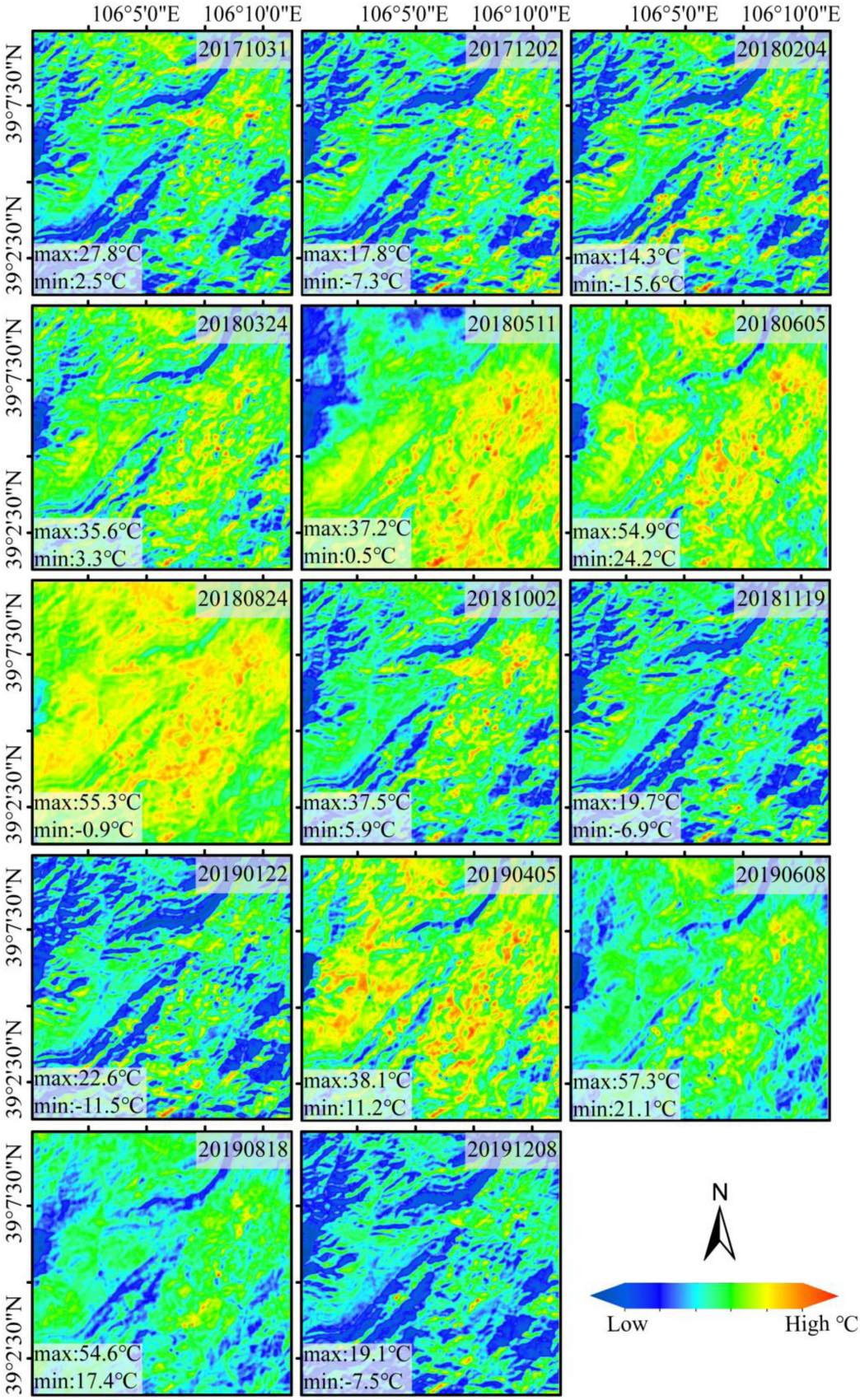

(b)

Fig. 5. *(Continued.)* (b) Results of surface temperature inversion using atmospheric correction algorithm for certain periods in the study area.

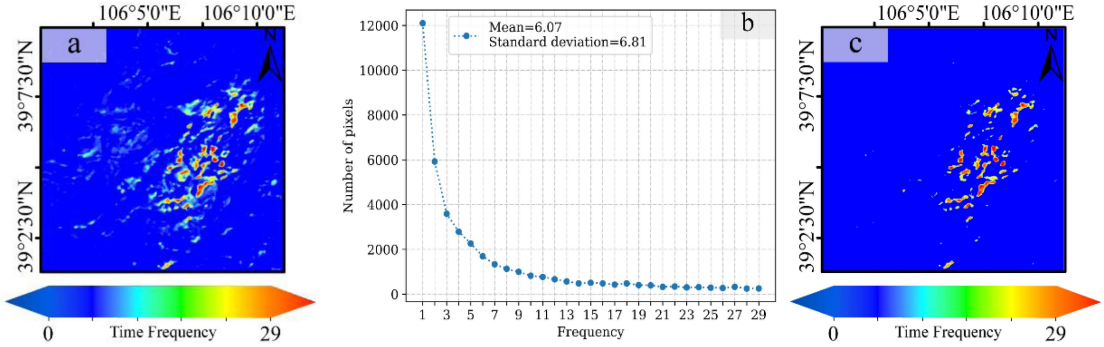

Fig. 6. Determining time-frequency thresholds. (a) Total time-frequency diagram. (b) Counting the number of pixels corresponding to different time frequencies and calculating the mean and standard deviation of the time frequencies. (c) Time-frequency image of $T_f = 13$.

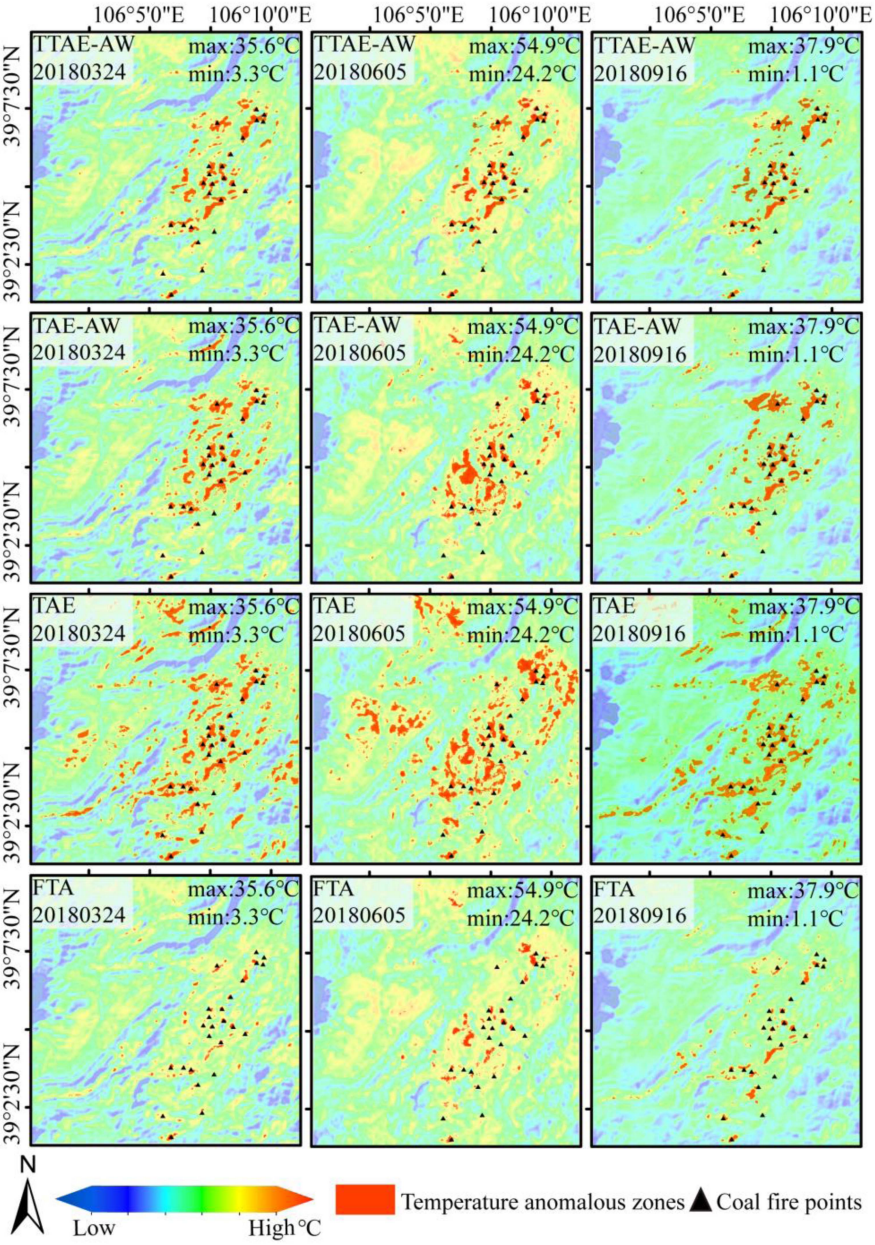

Fig. 7. Comparison of temperature anomalies extracted using different algorithms with coal fire point.

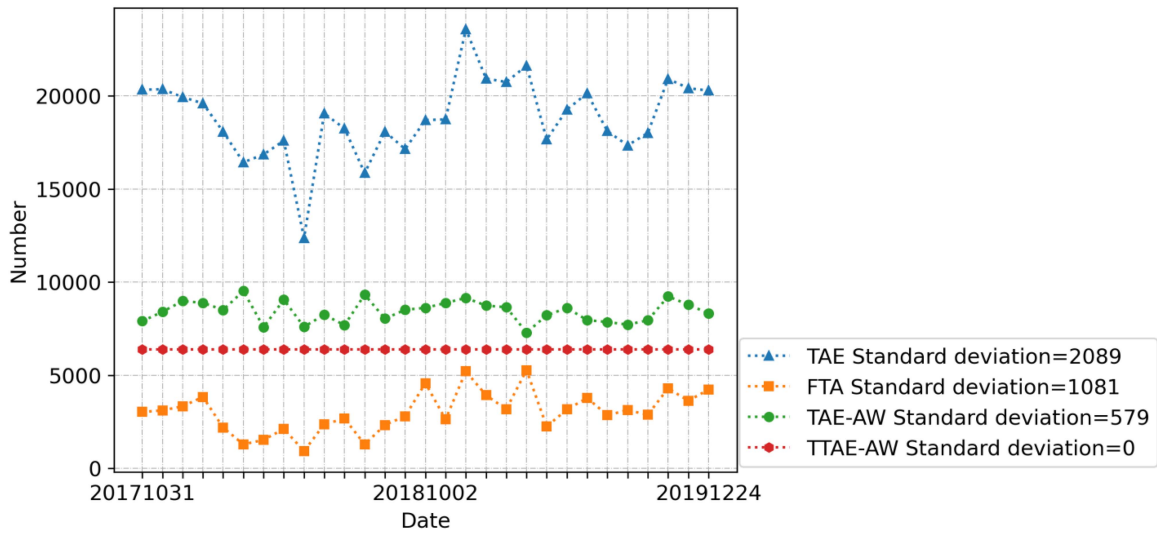

Fig. 8. Seasonal stability analysis. The number of temperature anomaly pixels and the corresponding standard deviation of the pixel numbers extracted for all images using the TTAE-AW, TAE-AW, TAE, and FTA methods.

frequencies of $>T_f$ are marked and such pixels are considered to be in coal fire zones. Pixels with time frequency of $<T_f$ do not conform to the coal fire burning time continuity law. Thus, they are considered not to belong to coal fire zones. Finally, through the steps of filtering the temperature anomaly images, retaining the location and temperature anomaly information of the marked pixels, and removing the unmarked pixels, the temporal temperature anomaly information is obtained (Fig. 2, Step5).

C. Method for Extracting Surface Deformation Anomalies

Time-series InSAR techniques, such as the persistent scatterer, small baseline (SB), and DS methods, can acquire high-precision, high-resolution, and wide-ranging surface deformation information, and they have been used widely in many fields [33], [34], [35], [36], [37], [38], [39], [40], [41], [42], [43], [44]. Compared with the persistent scatterer and SB techniques, the DS-InSAR technique can extract more coherent observation points by identifying statistically homogeneous pixels (SHPs) and estimating the optimal phase. In some low-coherence zones, such as coal mining zones and coal fire zones, the DS-InSAR technique has achieved favorable monitoring results due to its unique advantages [8], [12], [23], [24], [45], [46], [47]. Therefore, it was considered necessary in this article to use the DS-InSAR technique to extract surface deformation information. The main processes of the surface deformation anomaly extraction method include the following.

1) Generating Interferograms: The super master image is selected by overall correlation coefficient analysis. All auxiliary images are registered based on the super master image, and then they are resampled. Under the premise of ensuring no isolated points in the spatiotemporal baseline network, SB interferograms are constructed by setting vertical baseline and temporal baseline thresholds. Topographic contributions are simulated and removed using a digital elevation model (DEM).

2) Identifying Statistically Homogeneous Pixels (SHPs): SHP identification is one of the core algorithms of the DS-InSAR technique. SHP identification determines the degree of similarity between adjacent image elements and central image elements through statistical inference. The identification accuracy of the algorithm directly affects the accuracy of subsequently estimated parameters. In this article, the hypothesis test of confidence interval method proposed by Jiang et al. [48] was used to identify SHPs.

This method combines the merits of the fast statistical homogeneous pixel selection and the likelihood ratio test, and the unbiased estimate of the latter is used as the truth value of the reference pixels. At a preset confidence level, if the time-average intensity values of adjacent pixels fall into the truth-constructed interval, they are considered homogeneous samples of the reference pixels, which simultaneously guarantee the accuracy and speed of identifying statistically homogeneous points.

3) Estimating the Optimal Phase: The resolution cell of the DS is composed of multiple independent scatterers, which can cause decorrelation. Thus, to improve the density of points and the signal-to-noise ratio of the interferometric phase, an interferometric phase-optimization process is necessary after identification of SHPs. In this article, we adopted the eigendecomposition-based maximum likelihood estimator of the interferometric phase optimization algorithm proposed by Ansari et al. [49]. The method considers the high accuracy of the maximum likelihood method for estimating the covariance matrix, adopts the high efficiency of the eigenvalue decomposition solution strategy, and uses the coherence matrix as a weighting factor to suppress the effect of low-coherence interference pairs.

4) Selecting DS Points: The goodness of fit (γ_{TC}) between the original interference phase and the optimized phase, which is used as the evaluation index, can be expressed as follows:

$$\gamma_{\mathrm{TC}} = \frac{2}{N(N+1)} \mathrm{Re} \sum_{m=1}^{N} \sum_{n=m+1}^{N} e^{j\varphi_{m,n}} e^{-j(\theta_m - \theta_n)} \quad (5)$$

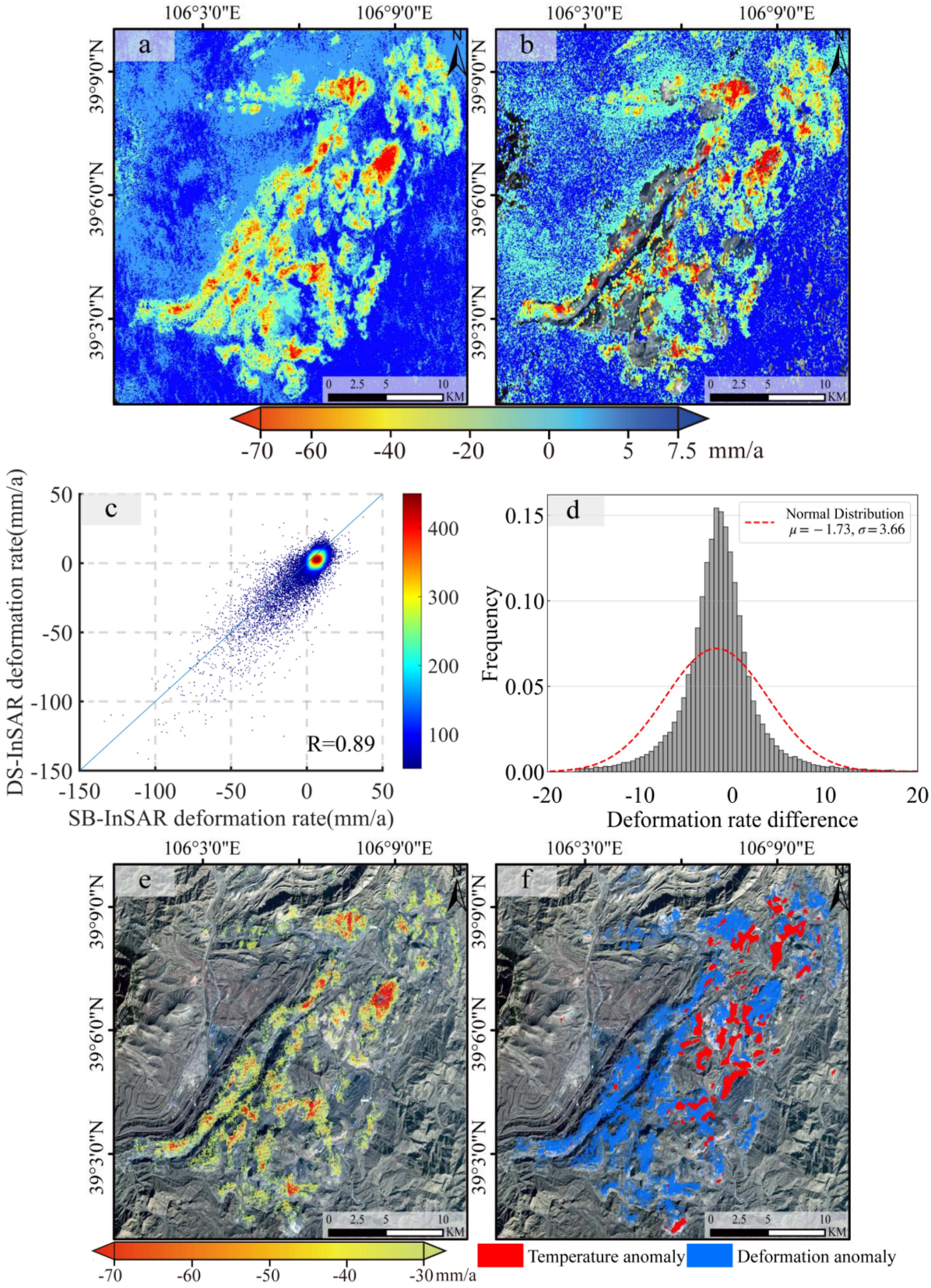

Fig. 9. Results of surface deformation monitoring of the Rujigou mining area. (a) Results of surface deformation rate in the LOS direction extracted using the DS-InSAR technique. (b) Results of surface deformation rate in the LOS direction extracted using the SB-InSAR technique. (c) Correlation coefficients of the two methods. (d) Histogram of deformation rate difference. (e) Results of surface deformation anomalies. (f) Results of overlaid analysis of time series temperature and deformation anomaly zones.

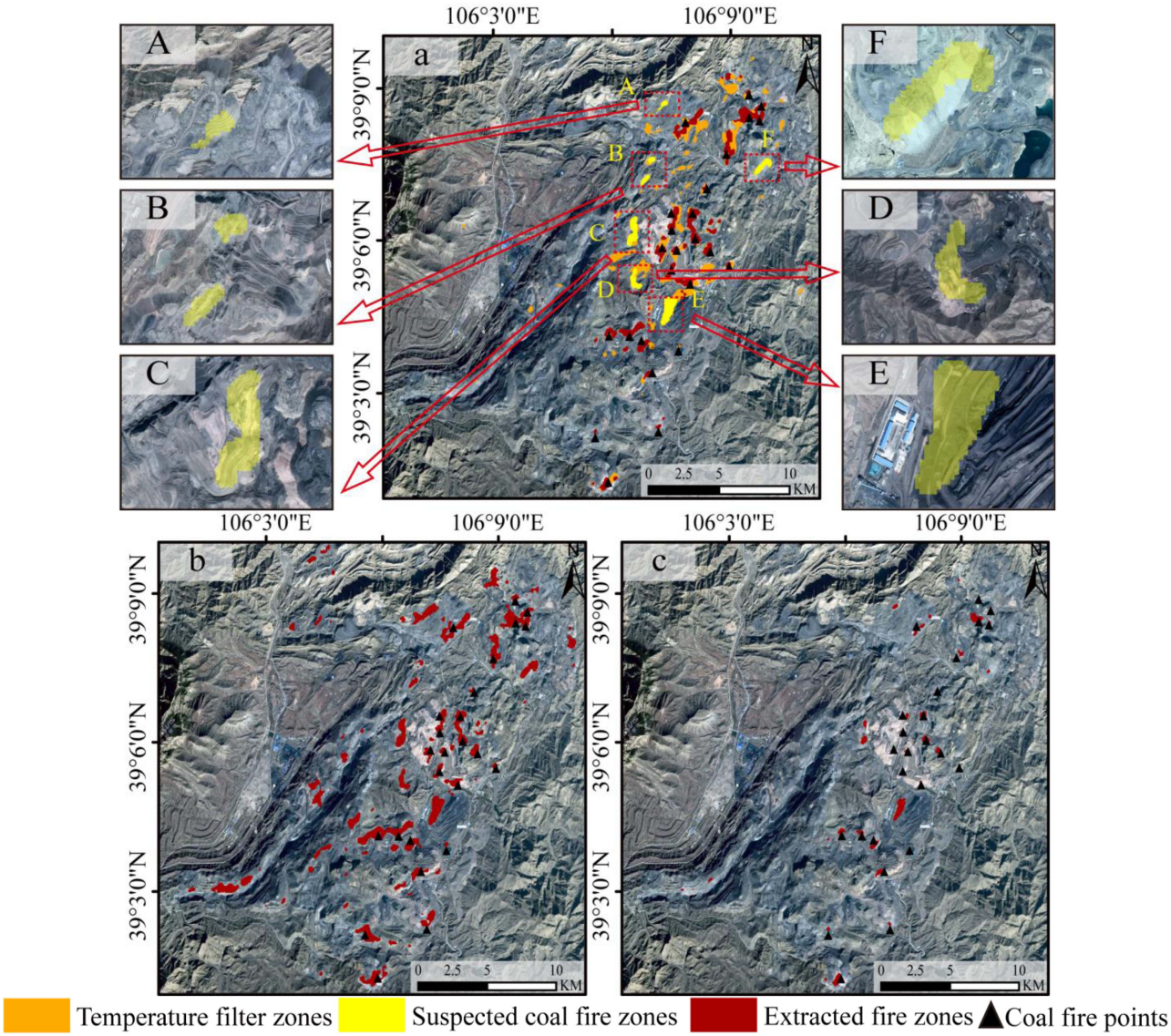

Fig. 10. Coal fire zone identification with combined temperature and deformation constraints. (a), (b), and (c) show the fire zone identification results obtained by the TTAE-AW +DS, TAE+DS, and FTA+DS methods, respectively.

where γ_{TC} is the goodness of fit index, N is the number of images, $\varphi_{m,n}$ represents the initial interferometric phase of the mth and nth SAR images, and θ_m and θ_n are the optimized phases of the reconstruction. Points with γ_{TC} values of >0.5 are selected as DS points.

5) Inverting the Surface Deformation Rate: The extracted DS points undergo three-dimensional phase unwrapping using StaMPS software. Then, the orbital residual errors, atmospheric delay errors, and DEM errors are evaluated and corrected. Finally, the surface deformation rate information of the DS points is solved using least squares estimation.

6) Extracting Surface Deformation Anomalies: The average surface deformation rate mean_{LOS} and its standard deviation σ_{LOS} are combined to extract the deformation anomaly

$$\text{Value}_{LOS} \leq \text{mean}_{LOS} - k \times |\sigma_{LOS}| \quad (6)$$

where Value_{LOS} is the deformation anomaly value and k is a positive number. Yu et al. [30] analyzed the influence of variation in the value of k on the extraction results of deformation anomalies. In this article, the best results were obtained for a value of $k = 2$.

D. Double-Threshold Two-Stage Filter (DTTF) Method

Based on the above extracted temperature and surface deformation time-series anomaly information, the DTTF algorithm is used to identify coal fire zones. The specific workflow of the algorithm is as follows (Fig. 3).

1) Overlaying Analysis: A window of suitable size (e.g., 4 × 4) is selected. The corresponding pixels of a temperature anomaly image [Fig. 3(a)] and a surface deformation anomaly image [Fig. 3(b)] are intersected by the window to obtain the intersection image [first-level filtering, Fig. 3(c)].

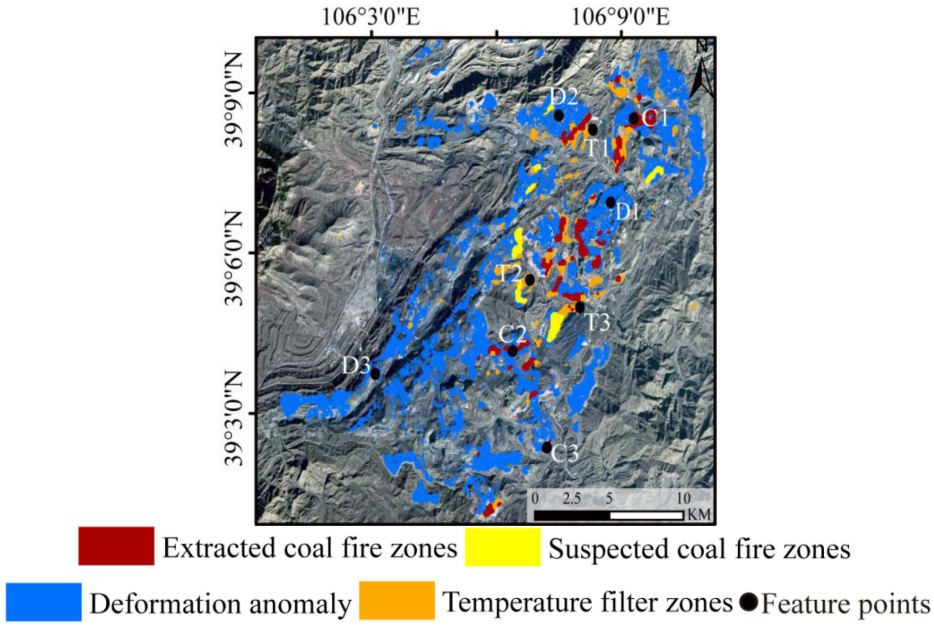

Fig. 11. Overview of the location of time-series feature points: *D*1, *D*2, and *D*3 are large deformation points; *T*1, *T*2, and *T*3 are high temperature points; and *C*1, *C*2, and *C*3 are coal fire points.

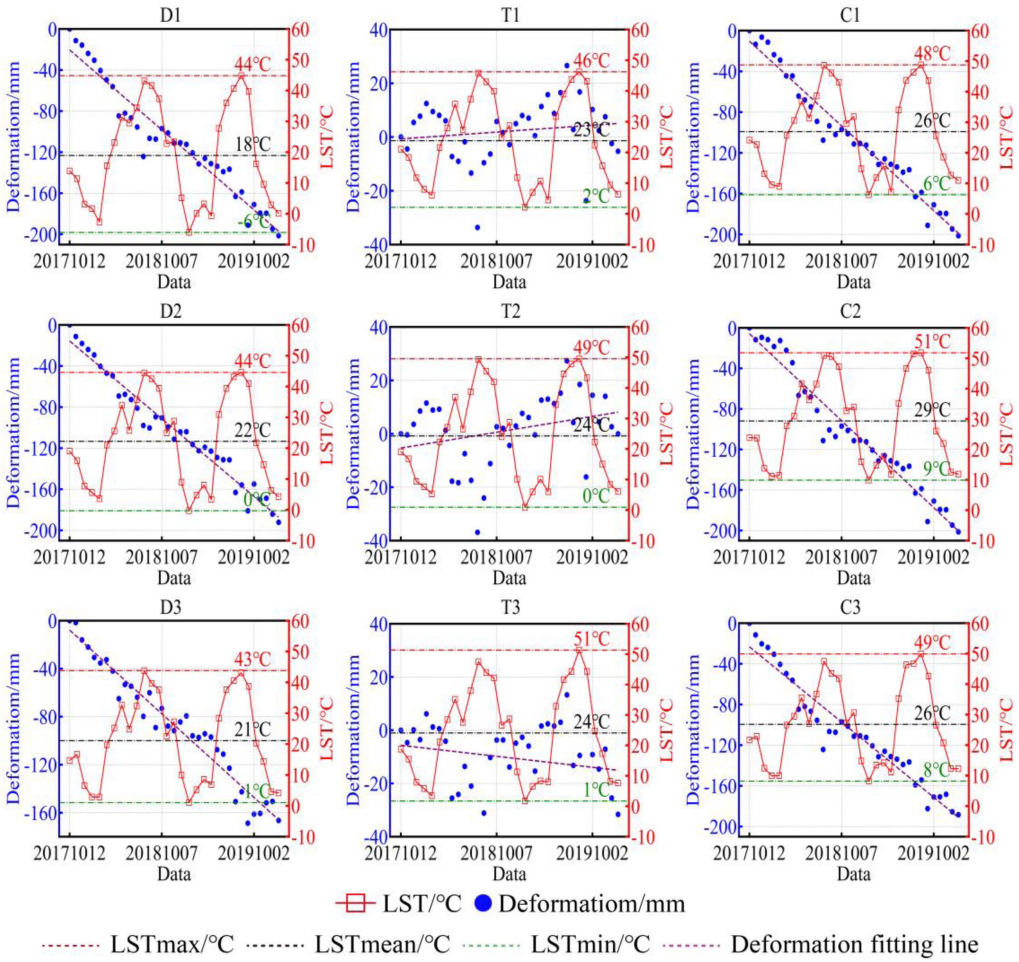

Fig. 12. Feature point time-series analysis.

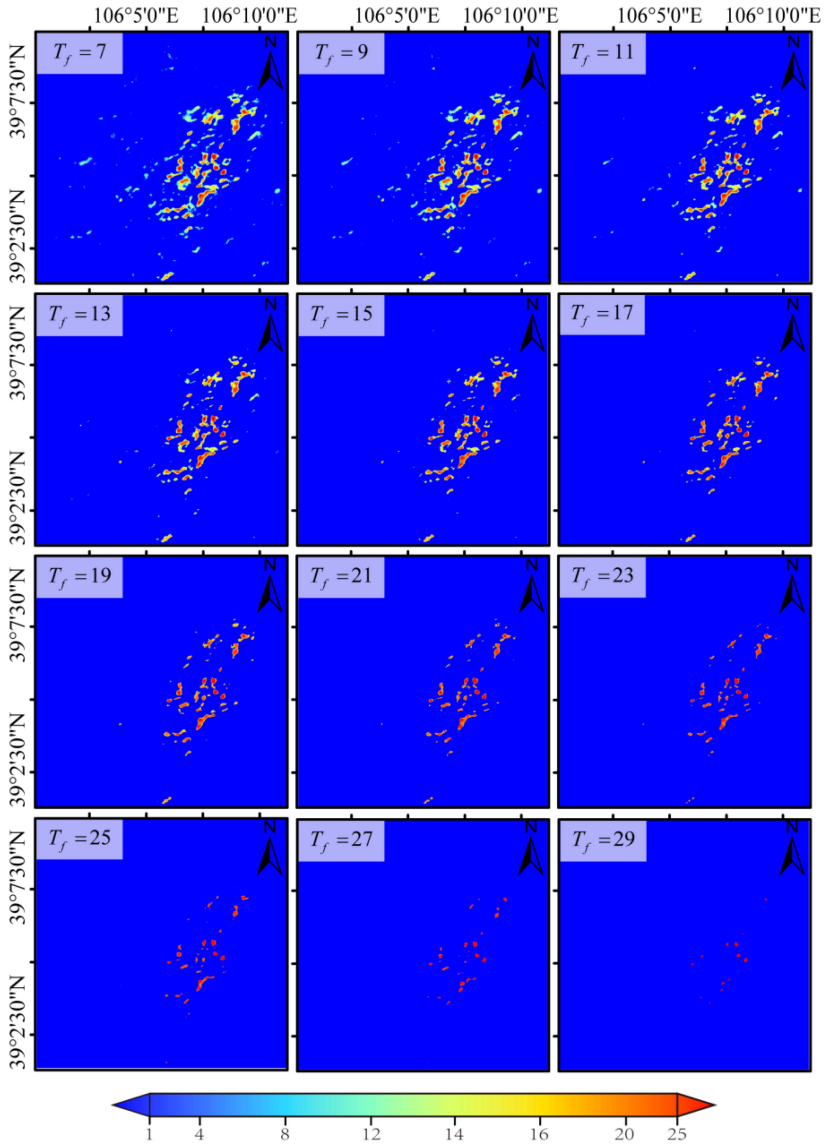

Fig. 13. Time-frequency images extracted with different time-frequency thresholds.

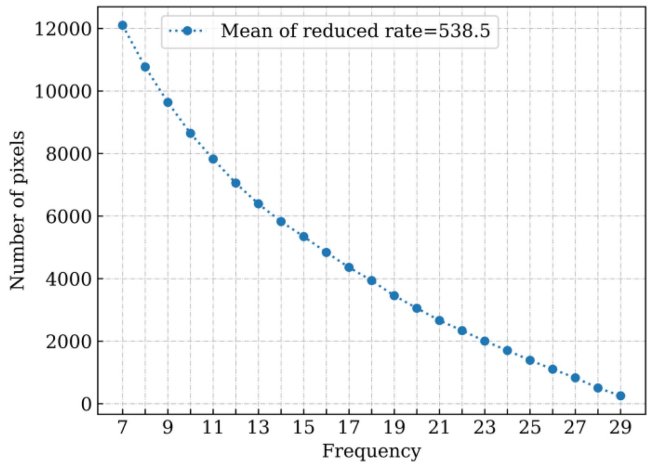

Fig. 14. Pixel reduction rate for different time-frequency thresholds.

2) Calculating the Loss Ratio (LR) and Determining the Double-Threshold Value: The loss ratio of a window is the ratio of the number of pixels lost by temperature anomalies after OA to the number of pixels lost by the original temperature anomalies. The mean and standard deviation of all window loss ratios are calculated, and the mean is used as the first threshold $T1$ and the mean plus standard deviation is used as the second threshold $T2$.

3) Identifying the Fire Zones: When LR $\leq T1$ for a window, the temperature anomaly is considered to match the deformation anomaly information and the intersection pixels within the window are retained. When LR $\geq T2$ for a window, the temperature anomaly is considered a mismatch with the deformation anomaly information and all image pixels in the window are discarded. When $T1 <$ LR $< T2$, it is considered that the temperature anomaly and deformation anomaly information match and therefore, the pixels in the corresponding window of the temperature anomaly image [Fig. 3(a)] are retained. Of

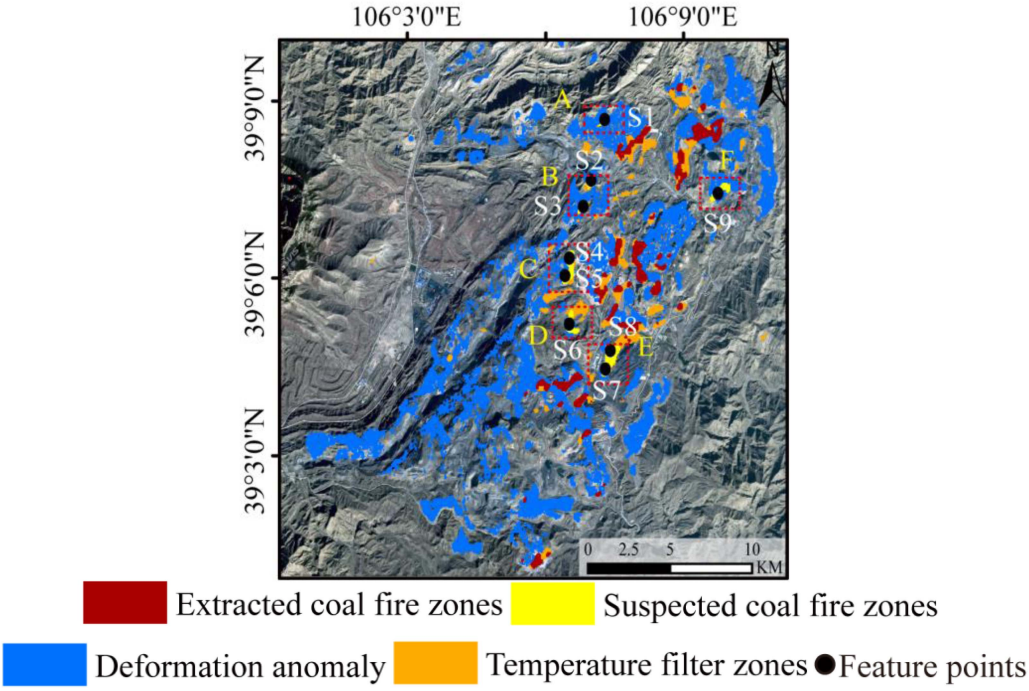

Fig. 15. Overview map of the location of time-series feature points in the suspected coal fire.

course, this rule was developed under the assumption that surface temperature is generally considered a more intuitive feature of coal fire burning than surface deformation among the multiple pixels that identify the fire zones. Finally, the fire zone identification image with the double-threshold constraint is obtained [Fig. 3(d)].

4) Filtering Independent Pixels: After applying the double-threshold constraint, a certain proportion of independent pixels will exist. Therefore, neighborhood analysis is performed to filter out pixels with fewer than three pixels in the eight-neighborhood range to obtain the final fire zone identification image [Fig. 3(e)].

III. Study Area and Datasets

A. Study Area

The Rujigou coal mining area is in the northern part of the Helan Mountains (average elevation: approximately 2000 m) in the Ningxia Hui Autonomous Region of China. It is one of the important bases of the coal mining industry in China. The main geological structure is a complex oblique belt consisting of several northeast-trending fractures and interphase back-slopes formed at the end of the Late Jurassic and Early Cretaceous [Fig. 4(a)]. The complex geological environment yields high-quality anthracite coal (Taixi coal), which is known as the king of coal globally. The coal fires in the Rujigou area began in the Ming and Qing dynasties. In the 1990s, large numbers of small- and medium-sized coal kilns were illegally mined leading to rapid spread of old coal fire zones and the creation of new coal fire zones. As of 2021, there were 25 coal fire zones caused by spontaneous combustion in coal seams and coal gangues in the Rujigou mining area [Fig. 4(b)] [50]. The total area affected is approximately 300 ha, with an annual loss of approximately 1.15 million tons of coal and direct economic losses of approximately 1 billion RMB. According to broad prediction, 311 million tons of high-quality anthracite coal in the Rujigou mining area will be lost in 50 years [50], [51].

B. Datasets

Overall, 29 Landsat-8 satellite images with $<10\%$ obscuration by cloud acquired from October 2017 to December 2019 were used to extract temperature anomaly information. Their spatial resolutions were 30 and 100 m in the visible (bands 1–7 and 9) and TIRs (bands 10 and 11), respectively (Table I).

The 35 C-band SAR images acquired by the Sentinel-1A satellite, launched by the Copernicus program of the European Space Agency, were used to extract surface deformation information. The images were acquired in the interferometric wide mode and the study period covered October 2017 to January 2020 (Table I).

The DEM, based on 30-m spatial resolution SRTM data measured jointly by NASA and the National Imagery and Mapping Agency, was used to remove the topographic phase from the time series differential interferometry. The European Space Agency provided precision orbital data.

IV. Results and Analysis

A. Surface Temperature Inversion Results

The results of the partial surface temperature inversion of the study area using the single-window algorithm are shown

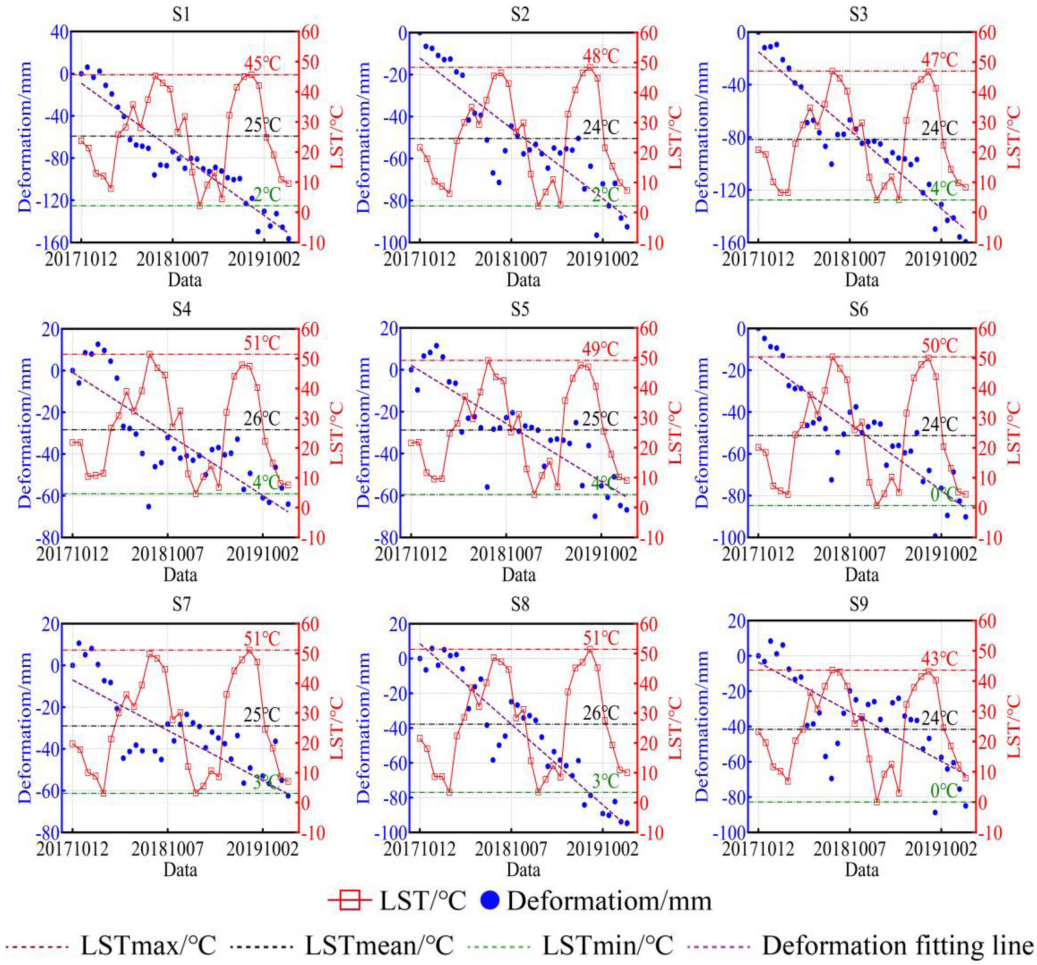

Fig. 16. Time-series analysis of the feature points in the suspected coal fire zones.

TABLE I
LANDSAT-8 AND SENTINEL-1A DATA

	Description	Description
Satellite name	Landsat - 8	Sentinel - 1A
Mode	OLI_TIRS	IW
Track	130 (129) / 33	157/122
Orbit direction	/	Ascending
Polarization	/	VV
Wavelength (m)	0.43-12.51	0.0555
Resolution (m)	30 (OLI) / 100 (TIRS)	5×20
Heading angle (°)	/	-9.78
Incidence angle (°)	/	39.1
Number of images	29	35
Time range	31 October 2017 - 24 December 2019	12 October 2017 - 6 January 2020

in Fig. 5(a). The results show that the temperature varied substantially both with season and with topographic undulation. The surface temperatures in the coal fire zones are noticeably higher than those in the surrounding zones in most periods. The noncoal fire zones in the northwest of the study area during individual periods (e.g., 20 180 824 and 20 190 405) have the same magnitude of temperature as the fire zones [as shown in the black rectangular box in Fig. 5(a)]. Thus, it is evident that the accuracy of relying only on temperature anomalies to identify fire zones is limited. To validate the reliability of the single-window algorithm, surface temperature inversion was carried out on the same datasets using the atmospheric correction method, and the results are shown in Fig. 5(b). The comparative analysis reveals that the temperature inversions of both methods

TABLE II
AVERAGE CONFUSION MATRIX OF OVERLAP BETWEEN TEMPERATURE ANOMALY EXTRACTION RESULTS AND COAL FIRE POINTS

TTAE-AW confusion matrix		Real data: Fire zones	Real data: Non-fire zones	User accuracy
Identification data	Fire zones	23	11	67.65%
	Non-fire zone	3	63	95.45%
Producer accuracy		88.46%	85.14%	
Total accuracy 0.86		Kappa 0.67		

TAE-AW confusion matrix		Real data: Fire zones	Real data: Non-fire zones	User accuracy
Identification data	Fire zones	23	16	58.97%
	Non-fire zones	3	58	95.08%
Producer accuracy		88.46%	78.38%	
Total accuracy 0.81		Kappa 0.58		

TAE confusion matrix		Real data: Fire zones	Real data: Non-fire zones	User accuracy
Identification data	Fire zones	24	32	42.86%
	Non-fire zones	2	42	91.30%
Producer accuracy		92.31%	56.76%	
Total accuracy 0.66		Kappa 0.36		

FTA confusion matrix		Real data: Fire zones	Real data: Non-fire zones	User accuracy
Identification data	Fire zones	10	9	52.63%
	Non-fire zones	16	65	80.25%
Producer accuracy		38.46%	87.84%	
Total accuracy 0.75		Kappa 0.29		

Note: A total of 100 points were randomly chosen in the study area and compared with the results of the temperature anomaly extraction.

are consistent in terms of magnitude and spatial distribution. The largest temperature difference of the same image inversion is 2.7 °C, and the root mean square error is 0.9 °C. Therefore, temperature anomaly information can be extracted using the results of the inversion of the single-window algorithm.

B. Time-Series Temperature Anomaly Extraction Results

The TAE and FTA methods were selected for comparison and analysis with the TTAE-AW and TAE-AW TAE algorithms proposed in this article. The TAE method uses windows of 11×11, 17×17, 29×29, and 35×35, and the window threshold is the first local minimum after the maximum value of the statistical histogram of temperature pixel values [27]. The window threshold selected by the FTA method is mean $+ 2\sigma$ [14], and the window thresholds chosen for the TTAE-AW and TAE-AW methods are mean $+ \sigma$and mean $+ 2\sigma$, respectively. To determine the time-frequency threshold T_f for the TTAE-AW method, the total time frequency of each pixel in the 29 temperature anomaly images extracted by the TAE-AW method was counted, and the total time-frequency diagram [Fig. 6(a)] and its histogram [Fig. 6(b)] were obtained. The average value of the total time frequency plus the standard deviation is used as T_f ($T_f = 13$). Then, the image with time frequency of >13 in the TAE-AW temperature anomaly map is retained [the pixel's position is as shown in Fig. 6(c)] to obtain the time-series temperature anomaly image.

Fig. 7 shows the results of the temperature anomalies extracted by the four methods for different periods (i.e., 20180324, 20180605, and 20180916). Fig. 8 shows the number of temperature anomaly pixels extracted by the four algorithms in all images and their standard deviations. Comprehensive analysis of Figs. 7 and 8 reveals that the number of temperature anomaly pixels extracted by the TAE method is much higher than that of the other methods. In terms of the spatial distribution, in addition to the temperature anomalies extracted in the fire zones, the temperature anomalies in the noncoal fire zones in other areas (northwest) were also extracted. This leads to the low accuracy of fire zone identification, especially the user accuracy (average user accuracy of fire zone identification for the 29 periods is 42.86%, Table II). The TAE method has the largest fluctuations in the spatial distribution and number of temperature anomalies in different seasons (standard deviation of the number of pixels is 2089, Fig. 8). This might be caused by the fixed window size and unstable temperature threshold. When the window is completely in the coal fire zones, it will lead to missed detection of temperature anomaly information. When the window is in the noncoal fire zones, it will lead to too much extracted temperature anomaly information owing to the instability of the threshold value. Thus, it is evident that the applicability of the TAE method is poor for the extraction of temperature anomalies in coal fire zones. The FTA method extracts the fewest temperature anomaly pixels. In terms of spatial distribution, this method is poor in extracting low-temperature anomaly zones at the edge of the fire zones and thus large numbers of fire zones will be missed. Its overall accuracy is moderate (mean value: 0.75) but the kappa coefficient is low (mean value: 0.29, Table II), which indicate that the mean $+ 2\sigma$ threshold of this method is not appropriate for this study area. In terms of seasonal stability, the FTA method is more stable than the TAE method and less stable than both the TTAE-AW method and the TAE-AW method (Fig. 8) The

TAE-AW method extracts temperature anomaly pixels using AWs and double thresholding. The TAE-AW method extracts fewer pixels than the TAE method but more than the FTA and TTAE-AW methods. Moreover, it is superior to the TAE and FTA methods in terms of accuracy and Kappa coefficient, and second only to the TTAE-AW method (Table II). It is also better than the TAE and FTA methods in terms of seasonal stability (Fig. 8). However, it also fails to consider the temporal continuity of coal fire combustion, resulting in the output containing more pixels of isolated temperature anomalies at specific points in time. The number of temperature anomaly pixels extracted by the TTAE-AW method is lower than that of the TAE-AW method and higher than that of the FTA method. The accuracy and kappa coefficient of identification of the TTAE-AW method were the highest among the four methods, i.e., 0.86 and 0.67, respectively (Table II), indicating that it is a more suitable extraction method for identifying temperature anomalies in fire zones because it filters stable temperature anomalies based on temporal continuity.

C. Surface Deformation and Anomaly Extraction Results

Fig. 9(a) shows the DS-InSAR monitoring results of surface deformation in the Rujigou mining area. To verify the reliability of DS-InSAR deformation monitoring results, the cross-validation approach was adopted using the SB-InSAR technique in StaMPS [Fig. 9(b)].

The SB-InSAR technique is configured with threshold parameters set at 60 days temporally and 200 m spatially. The results show that the number of coherent pixels extracted by the DS-InSAR technique is 608 896 and that the spatial coverage of the points is 158% better than that of the SB-InSAR technique.

The surface deformation obtained by DS-InSAR technique and SB-InSAR technique is dominated by subsidence, with maximum values of −146 and −150 mm/a and mean values of 2.63 and 1.26 mm/a, respectively. The spatial distribution of deformation rates is highly consistent. The selected 52 683 homonymous points were analyzed for correlation and differences. The results showed that the correlation coefficient was 0.89 [Fig. 9(c)]. The mean and standard deviation of deformation difference values are −1.73 and 3.66 mm/a, respectively [Fig. 9(d)], verifying the reliability and accuracy of the results.

Based on the results of DS-InSAR surface deformation monitoring, the deformation anomalies in the Rujigou mining area were extracted using the surface deformation anomaly information extraction method described in Section II-C. The result is shown in Fig. 9(e). Comparison of the temperature anomaly and the deformation anomaly [Fig. 9(f)] reveals clear intersection in the spatial distribution, but the deformation anomaly zones are more widely distributed than the temperature anomaly zones. The main reason is that both coal mining and spontaneous combustion of coal fires cause surface deformation; therefore, it is often impossible to accurately identify fire zones based on surface deformation alone. However, it can be used as a joint constraint with temperature anomaly information to identify fire zones, which can effectively weaken the misclassification phenomenon caused by the influence of solar radiation.

D. Results of Coal Fire Zone Identification

The DTTF method is used to identify fire zones by combining the temperature anomaly information extracted by the three methods of TTAE-AW, TAE, and FTA, and surface deformation anomaly information extracted as described in Section IV-D. To ensure the comparability of different algorithms, the temperature anomalies obtained by the TAE and FTA methods are processed as time series. The results were named TTAE-AW+DS, TAE+DS, and FTA+DS (Fig. 10). The resolution cell for the temperature anomaly image, surface deformation anomaly image, and the final intersection image are all 30 m × 30 m. The results show that the TAE+DS method identifies the largest range of fire zones and that the misclassification zones are largest [yellow area in Fig. 10(b)]. It has the lowest user accuracy of 62.86% in identifying fire zones (Table III).

The FTA+DS method is influenced by the FTA TAE results and it extracts the smallest and most scattered range of fire zones, although the user accuracy is higher (75%) and the misclassification rate is lower. However, the method misses too many fire zones, thereby resulting in the lowest producer accuracy of 23.08% [Fig. 10(c) and Table III]. Both the accuracy and the Kappa coefficient of the TTAE-AW method in identifying fire zones are the highest (i.e., 0.91 and 0.77, respectively), indicating that the extracted fire zones coincide with the locations of coal fire points [Fig. 10(a) and Table III].

According to Fig. 10(a), regions A, B, C, D, E, and F are tentatively identified as suspected coal fire zones. Combining a priori knowledge of the mining area and interpretation of Google images, it is evident that regions D and E are open-pit coal mines, whereas regions A, B, C, and F cannot be accurately identified in terms of their geographical profile. Region E is adjacent to the Rujigou coal mine, which was initially considered as a misjudged coal fire zone. Owing to the presence of both the large deformation and the long time series of high-temperature conditions in regions A, B, C, D, and F, it is impossible to determine whether these regions are misclassified coal fire zones. Therefore, it is necessary to select points in these regions to analyze the spatiotemporal characteristics of temperature and deformation (refer to Section V-B).

E. Time-Series Analysis of Feature Points for Joint Surface Temperature and Deformation

Three deformation feature points ($D1$, $D2$, and $D3$), three high-temperature points ($T1$, $T2$, and $T3$), and three underground coal fire points ($C1$, $C2$, and $C3$) in the study area were selected for time-series analysis (Figs. 11 and 12). Coal mining has caused subsidence at points $D1$ and $D2$, and the subsidence shows a linear relationship with time, whereas the deformation rate remains broadly constant. Point $D3$ is located on a road, which has subsided because of coal mining transportation. This subsidence also shows a linear relationship with time. However, because there are no high temperatures in this area, it is easy to rule it out based on temperature anomaly information. Because the fire zones of Rujigou have been under treatment, it can be observed that the predeformation rate is relatively fast and that the cumulative deformation volume is large at the coal fire

TABLE III
CONFUSION MATRIX OF FIRE ZONE IDENTIFICATION RESULTS AND COAL FIRE POINT OVERLAP BY DIFFERENT METHODS

TTAE-AW +DS confusion matrix		Real data: Fire zones	Real data: Non-fire zones	User accuracy
Identification data	Fire zones	22	5	81.48%
	Non-fire zone	4	69	94.52%
Producer accuracy		84.61%	93.24%	
Total accuracy 0.91		Kappa 0.77		

TAE+DS confusion matrix		Real data: Fire zones	Real data: Non-fire zones	User accuracy
Identification data	Fire zones	22	13	62.86%
	Non-fire zone	4	61	93.85%
Producer accuracy		84.61%	82.43%	
Total accuracy 0.83		Kappa 0.60		

FTA+DS confusion matrix		Real data: Fire zones	Real data: Non-fire zones	User accuracy
Identification data	Fire zones	6	3	75%
	Non-fire zone	20	72	78.26%
Producer accuracy		23.08%	97.28%	
Total accuracy 0.78		Kappa 0.26		

Note: A total of 100 points were randomly chosen in the study area and compared with the results of the temperature anomaly extraction.

TABLE IV
PIXEL REDUCTION RATE STATISTICS FOR EACH INTERVAL

Interval	7-8	8-9	9-10	10-11	11-12	12-13	13-14	14-15	15-16	16-17	17-18
Reduction rate	1334	1130	994	820	770	663	566	479	507	478	423
Interval	18-19	19-20	20-21	21-22	22-23	23-24	24-25	25-26	26-27	27-28	28-29
Reduction rate	481	402	393	323	337	299	312	289	272	325	250
Mean of reduction rate	538.5										

points $C1$, $C2$, and $C3$. The deformation rate is reduced after fire zone treatment. It is evident from Fig. 12 that the temporal temperatures of the $T1$, $T2$, and $T3$ points are higher than the temperatures of the three deformation points, but that there is no substantial subsidence in these areas and that the accumulated subsidence shows an irregular state. Therefore, assessment of the temporal deformation information can effectively remove such areas.

V. DISCUSSION

A. Time-Frequency Threshold Analysis

The selection of a suitable time-frequency threshold is crucial for accurate extraction of temporal temperature information.

Therefore, a time-frequency diagram [Fig. 6(a)] was calculated to obtain values of the $\text{mean}_{\text{LOS}} = 6.07$ and $\text{std} = 6.81$, and a time-frequency range of $7 \leq T_f \leq 29$ was selected (Fig. 13). Then, the time frequencies were divided into three ranges: $7 \leq T_f < 13$ (mean $\leq T_f <$ mean + std), $13 \leq T_f < 20$ (mean + std $\leq T_f <$ mean + 2 × std), and $T_f \geq 20$ ($T_f \geq$ mean + 2 × std). The temperature anomaly pixels show sharp reduction in the first range, followed by gradual decline in the second range, and further slower reduction in the third range. (Fig. 13). Fig. 14 and Table IV show the trend of pixel change under different time-frequency threshold intervals. It is evident that the rate of pixel reduction slows in each interval as the time-frequency increases. This is because the number of pixels falls as the time frequency increases. Therefore, it is not desirable to select the time-frequency threshold based on only one time-frequency threshold interval. First, the average pixel reduction rate of 22 time-frequency threshold intervals was calculated, $\text{Meanofreductionrate} = 538.5$. When the reduction rate is >538.5, it is the interval of a faster reduction rate, and when the reduction rate is <538.5, it is the interval of a slower reduction rate. When the time frequency is in the interval of a slower reduction rate. When the time frequency is in the interval

13–14 (Table IV), the pixel reduction rate broadly matches the average pixel reduction rate, and the results also match the range delineated in Fig. 13. Therefore $T_f = 13$ was considered an appropriate time-frequency threshold. The comprehensive analysis above is summarized as follows.

1) The time-frequency threshold cannot be selected based on a single time-frequency threshold interval because the selected threshold might be too high or too low, which would result in missing information on coal fire zones or retaining too many noncoal fire high-temperature zones.
2) As the time-frequency threshold increases, the temperature anomaly pixels decrease within a certain range at a faster rate and then at a slower rate. When the temporal frequency is in a low range, there will be large numbers of temporally irrelevant pixels. As the temporal frequency increases, large numbers of pixels will be removed and a smaller number of temporally relevant pixels will be retained. When the temporal frequency is in a high range, the rate of pixel reduction is slowed owing to the small base number of pixels associated with time. Therefore, the junction point where the pixel reduction rate is first fast and then slow is considered an appropriate time-frequency threshold.

B. Joint Time-Series Analysis of Surface Temperature and Deformation in Suspected Coal Fire Zones

To more accurately identify misclassified fire zones, nine feature points were selected in six regions (i.e., A, B, C, D, E, and F) for time-series analysis (Figs. 15 and 16). Analysis of points S1 and S9 in regions A and F reveals that the temperature data of these two points are low, i.e., the maximum temperature is 45 °C and 43 °C, respectively, which is different from the temperature of the underground coal fire zones. Therefore, it is judged that regions A and F are misjudged fire zones. Points S2, S3, S4, S5, and S6 have high temperature conditions and large deformation conditions that prevent accurate judgment. Therefore, regions B, C, and D are considered suspected coal fire regions and require caution. Points S7 and S8 in region E can be excluded based on interpretation of the Google images even though they have high-temperature conditions and large deformation conditions.

VI. Conclusion

In response to the problems of existing methods used for identification of coal fire zones, such as a high omission and misclassification ratio and lack of consideration of the time-series variation in surface temperature, this article proposed the TTAE-AW algorithm and DTTF method. Overall, 29 Landsat-8 images and 35 Sentinel-1A images were used to extract time-series information on temperature and deformation anomalies to realize identification of underground coal fire zones in the Rujigou mining area. The following conclusions were derived.

1) Compared with the TAE and FTA methods, the temperature anomaly zones extracted by the TTAE-AW method are more concentrated in the underground coal fire zones, and the number of temperature anomaly pixels extracted is more stable in different seasons. The average accuracy and Kappa coefficient of the TTAE-AW method were improved by 15.5% and 0.345 over the conventional method, respectively, indicating that the TTAE-AW method is more appropriate for extraction of temperature anomalies in underground coal fire zones.
2) Compared with the SB-InSAR approach, the DS-InSAR technique improves the spatial coverage of surface deformation monitoring points in coal fire zones by 158%, which is more helpful for identification of coal fire zones.
3) The accuracy and Kappa coefficient of the DTTF method combined with information of time-series temperature and deformation anomalies for identification of fire zones were 0.91 and 0.77, respectively, representing improvements of 5% and 0.1, respectively, compared with the results of the fire zone identification method relying on temperature anomaly information alone (i.e., the TTAE-AW method).

In summary, the active–passive remote sensing method proposed in this article for identification of underground coal fire zones with joint constraints of temperature and surface deformation time series can effectively identify and extract fire zones, thereby providing reliable technical support for coal fire monitoring and management.

Acknowledgment

The authors would like to thank the European Space Agency and the Geospatial Data Cloud for generously providing the Sentinel-1A SAR data, Precision orbital data, and Landsat-8 data.

References

[1] G. B. Stracher and T. P. Taylor, "Coal fires burning out of control around the world: Thermodynamic recipe for environmental catastrophe," *Int. J. Coal Geol.*, vol. 59, no. 1, pp. 7–17, Jul. 2004, doi: 10.1016/j.coal.2003.03.002.
[2] S. Voigt et al., "Integrating satellite remote sensing techniques for detection and analysis of uncontrolled coal seam fires in North China," *Int. J. Coal Geol.*, vol. 59, no. 1, pp. 121–136, Jul. 2004, doi: 10.1016/j.coal.2003.12.013.
[3] Y. J. Wang, "Research progress and prospect on ecological disturbance monitoring in mining area," *Acta Geodaetica et Cartographica Sinica*, vol. 46, no. 10, pp. 1705–1716, Oct. 2017, doi: 10.11947/j.AGCS.2017.20170358.
[4] Z. Y. Song and C. Kuenzer, "Coal fires in China over the last decade: A comprehensive review," *Int. J. Coal Geol.*, vol. 133, no. 1, pp. 72–99, Nov. 2014, doi: 10.1016/j.coal.2014.09.004.
[5] T. H. Syed, M. J. Riyas, and C. Kuenzer, "Remote sensing of coal fires in India: A review," *Earth-Sci. Rev.*, vol. 187, pp. 338–355, Dec. 2018, doi: 10.1016/j.earscirev.2018.10.009.
[6] S. S. Biswal, S. Raval, and A. K. Gorai, "Delineation and mapping of coal mine fire using remote sensing data—A review," *Int. J. Remote Sens.*, vol. 40, no. 17, pp. 6499–6529, 2019, doi: 10.1080/01431161.2018.1547455.
[7] J. J. Wu, W. G. Jiang, X. C. Liu, L. Gu, and J. H. Li, "Innovative technologies for exploration, monitoring and extinction of underground coal fires," *J. China Coal Soc.*, vol. 34, no. 12, pp. 1669–1674, Oct. 2009, doi: 10.3321/j.issn:0253-9993.2009.12.016.
[8] J. Liu et al., "Underground coal fires identification and monitoring using time-series InSAR with persistent and distributed scatterers: A case study of Miquan coal fire zone in Xinjiang, China," *IEEE Access*, vol. 7, pp. 164492–164506, 2019, doi: 10.1109/ACCESS.2019.2952363.
[9] Z. L. Shao et al., "Detection, extinguishing, and monitoring of a coal fire in Xinjiang, China," *Environ. Sci. Pollut. Res.*, vol. 25, no. 26, pp. 26603–26616, Jul. 2018, doi: 10.1007/S11356-018-2715-6.

[10] J. Kim, S. Y. Lin, R. P. Singh, C. W. Lan, and H. W. Yun, "Underground burning of Jharia coal mine (India) and associated surface deformation using InSAR data," *Int. J. Appl. Earth Observ. Geoinf.*, vol. 103, pp. 102524–102535, Dec. 2021, doi: 10.1016/j.jag.2021.102524.

[11] Z. Shao, Y. Liang, F. Tian, S. Song, and R. Deng, "Constructing 3-D land surface temperature model of local coal fires using UAV thermal images," *IEEE Trans. Geosci. Remote Sens.*, vol. 60, May 2022, Art. no. 5002309, doi: 10.1109/TGRS.2022.3176854.

[12] Y. J. Wang et al., "Research on multi-source remote sensing detection of concealed fire sources in coalfields," *Geomatics Inf. Sci. Wuhan Univ.*, vol. 47, no. 10, pp. 1651–1661, Oct. 2022, doi: 10.13203/j.whugis20220184.

[13] W. G. Jiang, J. J. Wu, L. Gu, X. C. Liu, and X. L. Li, "Change monitoring in Wuda coalfield fire area based on remote sensing," *J. China Coal Soc.*, vol. 35, no. 6, pp. 964–968, Jun. 2010, doi: 10.13225/j.cnki.jccs.2010.06.028.

[14] W. G. Jiang, J. J. Wu, L. Gu, B. Yang, Q. Chen, and X. C. Liu, "Monitoring method of underground coal fire based on night thermal infrared remote sensing technology," *Spectrosc. Spectral Anal.*, vol. 31, no. 2, pp. 357–361, Feb. 2011, doi: 10.3964/j.issn.1000-0593(2011)02-0357-05.

[15] Q. Xia and Z. Q. Hu, "A novel method to monitor coal fires based on multi-spectral Landsat images," *Spectrosc. Spectral Anal.*, vol. 36, no. 8, pp. 2712–2720, 2016, doi: 10.3964/j.issn.1000-0593(2016)08-2712-09.

[16] V. Karanam, M. Motagh, S. Garg, and K. Jain, "Multi-sensor remote sensing analysis of coal fire induced land subsidence in Jharia Coalfields, Jharkhand, India," *Int. J. Appl. Earth Observ. Geoinf.*, vol. 102, pp. 102439–102453, Oct. 2021, doi: 10.1016/j.jag.2021.102439.

[17] R. Ghosh, P. K. Gupta, V. Tolpekin, and S. K. Srivastav, "An enhanced spatiotemporal fusion method—Implications for coal fire monitoring using satellite imagery," *Int. J. Appl. Earth Observ. Geoinf.*, vol. 88, pp. 102056–102070, Jun. 2020, doi: 10.1016/j.jag.2020.102056.

[18] Y. X. Zhao et al., "Identification of mining induced ground fissures using UAV and infrared thermal imager: Temperature variation and fissure evolution," *ISPRS J. Photogrammetry Remote Sens.*, vol. 180, pp. 45–64, Oct. 2021, doi: 10.1016/j.isprsjprs.2021.08.005.

[19] X. Chen, J. Peng, Z. Song, Y. Zheng, and B. Zhang, "Monitoring persistent coal fire using landsat time series data from 1986 to 2020," *IEEE Trans. Geosci. Remote Sens.*, vol. 60, 2022, Art. no. 5001616, doi: 10.1109/TGRS.2022.3142350.

[20] Z. Y. Song et al., "Analysis of coal fire dynamics in the Wuda syncline impacted by fire-fighting activities based on in-situ observations and Landsat-8 remote sensing data," *Int. J. Coal Geol.*, vol. 141/142, pp. 91–102, Mar. 2015, doi: 10.1016/j.coal.2015.03.008.

[21] G. Yuan et al., "Accuracy assessment and scale effect investigation of UAV thermography for underground coal fire surface temperature monitoring," *Int. J. Appl. Earth Observ. Geoinf.*, vol. 102, pp. 102426–102442, Oct. 2021, doi: 10.1016/j.jag.2021.102426.

[22] T. R. Martha, A. Guha, K. V. Kumar, M. V. V. Kamaraju, and E. V. R. Raju, "Recent coal-fire and land-use status of Jharia coalfield, India from satellite data," *Int. J. Remote Sens.*, vol. 31, no. 12, pp. 3243–3262, Jun. 2010, doi: 10.1080/01431160903159340.

[23] J. L. Liu, Y. J. Wang, S. Y. Yan, L. B. Dang, F. Feng, and Y. Li, "Multi-source remote sensing fusion detection of coal fire in Eastern Urumchi," *Saf. Coal Mines*, vol. 50, no. 8, pp. 158–161, Aug. 2019, doi: 10.13347/j.cnki.mkaq.2019.08.039.

[24] J. L. Liu et al., "Underground coal fire detection and monitoring based on Landsat-8 and Sentinel-1 data sets in Miquan fire area, Xinjiang," *Remote Sens.*, vol. 13, no. 6, pp. 1141–1165, Mar. 2021, doi: 10.3390/rs13061141.

[25] X. M. Du, D. Y. Cao, D. Mishra, S. Bernardes, T. R. Jordan, and M. Madden, "Self-adaptive gradient-based thresholding method for coal fire detection using ASTER thermal infrared data, part I: Methodology and decadal change detection," *Remote Sens.*, vol. 7, no. 6, pp. 6576–6610, May 2015, doi: 10.3390/rs70606576.

[26] T. Wang et al., "A spatio-temporal temperature-based thresholding algorithm for underground coal fire detection with satellite thermal infrared and radar remote sensing," *Int. J. Appl. Earth Observ. Geoinf.*, vol. 110, pp. 102805–102816, Jun. 2022, doi: 10.1016/j.jag.2022.102805.

[27] C. Kuenzer, J. Zhang, J. Li, H. Mehl, and W. Wagner, "Detecting unknown coal fires: Synergy of automated coal fire risk area delineation and improved thermal anomaly extraction," *Int. J. Remote Sens.*, vol. 28, no. 20, pp. 4561–4585, Sep. 2007, doi: 10.1080/01431160701250432.

[28] S. Y. Yan, K. Shi, Y. Li, J. L. Liu, and H. F. Zhao, "Integration of satellite remote sensing data in underground coal fire detection: A case study of the Fukang region, Xinjiang, China," *Front. Earth Sci.*, vol. 14, no. 1, pp. 1–12, 2000, doi: 10.1007/s11707-019-0757-9.

[29] J. Hoffmann, A. Roth, and S. Voigt, "Detecting coal fires in China using differential interferometric synthetic aperture radar (InSAR)," *Nucleosides, Nucleotides Nucleic Acids*, vol. 29, no. 4, pp. 408–413, 2004, doi: 10.1080/15257771003730078.

[30] B. Yu et al., "Coal fire identification and state assessment by integrating multitemporal thermal infrared and InSAR remote sensing data: A case study of Midong district, Urumqi, China," *ISPRS J. Photogrammetry Remote Sens.*, vol. 190, pp. 144–164, Aug. 2022, doi: 10.1016/j.isprsjprs.2022.06.007.

[31] Y. Gao, G. Sui, X. J. Zhang, J. Y. Kong, and H. S. Zhang, "Application of remote sensing method in coal fire identification in Ningwu Coalfield," *Coal Sci. Technol.*, vol. 51, no. 5, pp. 133–139, May 2023, doi: 10.13199/j.cnki.cst.2021-1461.

[32] Z. H. Qin, M. H. Zhang, K. Arnon, and B. Pedro, "Mono-window algorithm for retrieving land surface temperature from Landsat TM6 data," *Acta Geographica Sinica*, vol. 56, no. 4, pp. 456–466, Apr. 2001, doi: 10.11821/xb200104009.

[33] A. Ferretti, C. Prati, and F. Rocca, "Nonlinear subsidence rate estimation using permanent scatterers in differential SAR interferometry," *IEEE Trans. Geosci. Remote Sens.*, vol. 38, no. 5, pp. 2202–2212, Sep. 2000, doi: 10.1109/36.868878.

[34] A. Ferretti, C. Prati, and F. Rocca, "Permanent scatterers in SAR interferometry," *IEEE Trans. Geosci. Remote Sens.*, vol. 39, no. 1, pp. 8–20, Jan. 2001, doi: 10.1109/36.898661.

[35] A. Hooper, "A multi-temporal InSAR method incorporating both persistent scatterer and small baseline approaches," *Geophys. Res. Lett.*, vol. 35, no. 16, pp. 96–106, Aug. 2008, doi: 10.1029/2008gl034654.

[36] A. Hooper, D. Bekaert, K. Spaans, and M. Arikan, "Recent advances in SAR interferometry time series analysis for measuring crustal deformation," *Tectonophysics*, vol. 514, pp. 1–13, Jan. 2012, doi: 10.1016/j.tecto.2011.10.013.

[37] P. Berardino, G. Fornaro, R. Lanari, and E. Sansosti, "A new algorithm for surface deformation monitoring based on small baseline differential SAR interferograms," *IEEE Trans. Geosci. Remote Sens.*, vol. 40, no. 11, pp. 2375–2383, Nov. 2002, doi: 10.1109/TGRS.2002.803792.

[38] M. Jiang, X. L. Ding, R. F. Hanssen, R. Malhotra, and L. Chang, "Fast statistically homogeneous pixel selection for covariance matrix estimation for multitemporal InSAR," *IEEE Trans. Geosci. Remote Sens.*, vol. 53, no. 3, pp. 1213–1224, Mar. 2015, doi: 10.1109/TGRS.2014.2336237.

[39] Y. Chen et al., "Long-term ground displacement observations using InSAR and GNSS at Piton de la Fournaise volcano between 2009 and 2014," *Remote Sens. Environ.*, vol. 194, pp. 230–247, Jun. 2017, doi: 10.1016/j.rse.2017.03.038.

[40] Y. Chen, Y. Tong, and K. Tan, "Coal mining deformation monitoring using SBAS-InSAR and offset tracking: A case study of Yu County, China," *IEEE J. Sel. Topics Appl. Earth Observ. Remote Sens.*, vol. 13, pp. 6077–6087, Oct. 2020, doi: 10.1109/jstars.2020.3028083.

[41] B. Q. Chen et al., "Three-dimensional time-varying large surface displacements in coal exploiting areas revealed through integration of SAR pixel offset measurements and mining subsidence model," *Remote Sens. Environ.*, vol. 240, Apr. 2020, Art. no. 111663, doi: 10.1016/j.rse.2020.111663.

[42] B. Q. Chen, H. Mei, Z. H. Li, Z. S. Wang, Y. Yu, and H. Yu, "Retrieving three-dimensional large surface displacements in coal mining areas by combining SAR pixel offset measurements with an improved mining subsidence model," *Remote Sens.*, vol. 13, no. 13, 2021, Art. no. 2541, doi: 10.3390/rs13132541.

[43] B. Q. Chen et al., "Time-varying surface deformation retrieval and prediction in closed mines through integration of SBAS InSAR measurements and LSTM algorithm," *Remote Sens.*, vol. 14, no. 3, 2022, Art. no. 788, doi: 10.3390/rs14030788.

[44] B. Q. Chen et al., "A new sequential homogeneous pixel selection algorithm for distributed scatterer InSAR," *GIsci. Remote Sens.*, vol. 60, no. 1, 2023, Art. no. 2218261, doi: 10.1080/15481603.2023.2218261.

[45] Y. Chen et al., "Revealing land surface deformation over the Yineng backfilling mining area, China, by integrating distributed scatterer SAR interferometry (DS InSAR) and a mining subsidence model," *IEEE J. Sel. Topics Appl. Earth Observ. Remote Sens.*, vol. 16, pp. 3611–3634, Mar. 2023, doi: 10.1109/jstars.2023.3250419.

[46] C. Zhao, Z. Li, B. Tian, P. Zhang, and Q. Chen, "A ground surface deformation monitoring InSAR method using improved distributed scatterers phase estimation," *IEEE J. Sel. Topics Appl. Earth Observ. Remote Sens.*, vol. 12, no. 11, pp. 4543–4553, Nov. 2019, doi: 10.1109/JSTARS.2019.2946729.

[47] G. Shi, H. Lin, and P. Ma, "A hybrid method for stability monitoring in low-coherence urban regions using persistent and distributed scatterers," *IEEE J. Sel. Topics Appl. Earth Observ. Remote Sens.*, vol. 11, no. 10, pp. 3811–3821, Oct. 2018, doi: 10.1109/JSTARS.2018.2867832.
[48] M. Jiang, X. L. Ding, and Z. W. Li, "Homogeneous pixel selection algorithm for multitemporal InSAR," *Chin. J. Geophys.*, vol. 61, no. 12, pp. 10–18, Dec. 2018, doi: 10.6038/cjg2018L0490.
[49] H. Ansari, F. D. Zan, and R. Bamler, "Efficient phase estimation for interferogram stacks," *IEEE Trans. Geosci. Remote Sens.*, vol. 56, no. 7, pp. 4109–4125, Jul. 2018, doi: 10.1109/tgrs.2018.2826045.
[50] J. H. Wang and B. L. Chen, "Fire zone governance and monitoring method selection and application in Rujigou coalmine area," *Coal Geol. China*, vol. 33, no. 11, pp. 81–86, Nov. 2021, doi: 10.3969/j.issn.1674-1803.2021.11.16.
[51] H. Wang, Y. Liu, X. F. Tang, and W. Wang, "Rapid treatment technology of small coal mine fire district in Rujigou open pit mine," *Coal Technol.*, vol. 35, no. 1, pp. 164–166, 2016, doi: 10.13301/j.cnki.ct.2016.01.063.

Yu Chen received the master's degree in photogrammetry and remote sensing from the China University of Mining and Technology (CUMT), Xuzhou, China, in 2012, and the Ph.D. degree in earth and planetary science from the University of Toulouse, Toulouse, France, in 2017.

She was an Assistant Researcher with the Géoscience Environnement Toulouse Laboratory, French National Center for Scientific Research, in 2013. She is currently an Associate Professor with the CUMT. Her research interests include SAR interferometry, with particular emphasis on its application for geophysical studies.

Zhihui Suo received the B.E. degree in surveying and mapping engineering from the Henan Polytechnic University, Jiaozuo, China, in 2021.

He is currently a Graduate Student majoring in surveying and mapping engineering with the China University of Mining and Technology, Xuzhou, China. His research interests include identification of underground coal fires and inversion of cavity parameters.

Jie Li received the M.S. degree in surveying and mapping engineering from the China University of Mining and Technology, Xuzhou, China, in 2023. He is currently working toward the doctoral degree in surveying and mapping with the Chang'an University, Xi'an, China.

His research interests include synthetic aperture radar interferometry.

Jun Wei received the B.E. degree in surveying and mapping engineering from the Xi'an University of Science and Technology, Xian, China, in 1995.

He is currently a Senior Engineer with the Xinjiang Uygur Autonomous Region Mine Safety Service and Guarantee Center, Urumqi, China. His research interests include technical management of mine safety.

Fei Cao received the B.E. degree in surveying and mapping engineering from the Chengdu University of Technology, Chengdu, China, in 2008.

He is currently a Senior Engineer with the Xinjiang Uygur Autonomous Region Mine Safety Service and Guarantee Center, Urumqi, China. His research interests include surveying and preventing underground coal fires.

Huahai Sun received the B.E. degree in resource exploration engineering from the Xinjiang University, Urumqi, China, in 2009.

He is currently a Senior Engineer with the Xinjiang Uygur Autonomous Region Mine Safety Service and Guarantee Center, Urumqi, China. His research interests include prevention and early warning of coalfield fires.

Huaizhan Li received the Ph.D. degree in geodesy and surveying engineering from the China University of Mining and Technology (CUMT), Xuzhou, China, in 2017.

He was a Postdoctoral Teacher with the School of Environment and Spatial Informatics, CUMT, in 2007. He is currently an Associate Professor with the CUMT. His research interests include deformation monitoring and subsidence control, with particular emphasis on its application for coal mine.

Yandong Gao received the B.S. and M.S. degrees in survey and mapping engineering from the University of Science and Technology Liaoning, Anshan, China, in 2013 and 2016, respectively, and the Ph.D. degree in geodesy and surveying engineering from the School of Environment Science and Spatial Informatics, China University of Mining and Technology, Xuzhou, China, in 2019.

He is currently an Associate Professor with the School of Environment Science and Spatial Informatics, China University of Mining and Technology. His research interests include the fields of interferometric phase filtering, phase unwrapping, and synthetic aperture radar interferometry signal processing and applications.

Qian Li received the B.E. degree in surveying and mapping engineering from the Shandong University of Science and Technology, Taian, China, in 2021.

She is currently a Graduate Student majoring in surveying and mapping engineering with the China University of Mining and Technology, Xuzhou, China. Her research interest includes synthetic aperture radar interferometry.

Yinglong Yue received the B.E. degree in geographical information science from the China University of Mining and Technology, Xuzhou, China, in 2010.

He was employed with the Ningxia Baoneng Coalfield Fire Extinguishing Engineering Company Limited, from 2010 to 2014. He is currently working with the Ningxia Coal Institute Company Limited. His research interest includes engineering surveying and mapping.

Kaimin Xu received the B.E. degree in geographical information science from the China University of Mining and Technology, Xuzhou, China, in 2010.

He is currently the General Manager with the Shaanxi Star Times Technology Development Company Limited, Xian, China. His research interests include geographic information, aerial remote sensing, digital twins, satellite positioning, cloud platforms, and image recognition (AI).